

**ANALYTICAL AND NUMERICAL SOLUTIONS OF
GENERALIZED FOKKER-PLANCK EQUATIONS**

Anil K. Prinja, PI
Chemical and Nuclear Engineering Department
The University of New Mexico
Albuquerque, NM 87131 USA

FINAL REPORT

DOE PROJECT DE-FG07-98ID13634

1 Introduction

The overall goal of this project was to develop advanced theoretical and numerical techniques to quantitatively describe the spreading of a collimated beam of charged particles in space, in angle, and in energy, as a result of small deflection, small energy transfer Coulomb collisions with the target nuclei and electrons. Such beams arise in several applications of great interest in nuclear engineering, and include electron and ion radiotherapy, ion beam modification of materials, accelerator transmutation of waste, and accelerator production of tritium, to name some important candidates. These applications present unique and difficult modeling challenges, but from the outset are amenable to the language of “transport theory”, which is very familiar to nuclear engineers and considerably less-so to physicists and material scientists. Thus, our approach has been to adopt a fundamental description based on transport equations, but the forward peakedness associated with charged particle interactions precludes a direct application of solution methods developed for neutral particle transport. Unique problem formulations and solution techniques are necessary to describe the transport and interaction of charged particles. In particular, we have developed the Generalized Fokker-Planck (GFP) approach to describe the angular and radial spreading of a collimated beam and a renormalized transport model to describe the energy-loss straggling of an initially monoenergetic distribution. Both analytic and numerical solutions have been investigated and in particular novel finite element numerical methods have been developed.

In the first phase of the project, asymptotic methods were used to develop closed form solutions to the GFP equation for different orders of expansion, and was described in a previous progress report. In this final report we present a detailed description of (i) a novel energy straggling model based on a Fokker-Planck approximation but which is adapted for a multigroup transport setting, and (ii) two unique families of discontinuous finite element schemes, one linear and the other nonlinear.

2 Interaction Physics

Charged particles interact through spherically symmetric Coulomb forces, and are affected by electronic screening of the nuclear charge. The interatomic potential between incident particle and the target atom can be expressed as

$$V(r) = \phi(r) \frac{Z_p Z_m e^2}{r} \left(\frac{esu^2}{cm} \right) \quad (1)$$

where e is the electron charge, r the distance between the particle of the atomic number Z_p and the target material nucleus of atomic number Z_m . The $\phi(r)$ is a screening function that can be represented by various models. At high energies screening is unimportant so that $\phi(r) = 1$, which is just the Rutherford model [1]. From the interatomic potential interaction cross sections and energy loss parameteres can be derived. In particular, the mean and mean-square energy loss per path length in the material are important to our work and are described below.

2.1 Mean Energy Loss

The predominant energy loss mode for high energy charged particles is through inelastic electronic collisions which results in ionization and excitation of the material. What is unique about this energy loss process is the high density of the electrons in the target material and long range of the Coulomb forces makes the frequency of the collisions numerous, but the fractional energy lost by the incident particle per collision is very small. This allows for a simpler description of the energy loss process through averages rather than the distributions.

For a quantum mechanical treatment collisions can be separated into hard and soft [2]. A hard collision is an interaction in which the electron can be regarded as initially free. The relativstic Rutherford cross section for heavy

charged particles that accounts for only the hard collisions is given by [2]

$$\Sigma(E, Q) = \frac{2\pi Z_p^2 e^4}{m_0 c^2 \beta^2} \frac{NZ}{Q^2} \left(1 - \beta^2 \frac{Q}{Q_{max}} \right) \quad (2)$$

where E is the incident ion energy, Q is the energy lost by the incident particle per collision, and Q_{max} is the maximum energy that can be transferred. The latter is well approximated by

$$Q_{max} \approx 1.022 \beta^2 \gamma^2 \quad (3)$$

where β is the ratio of the ion speed to the speed of light, and

$$\gamma^2 = \frac{1}{1 - \beta^2} \quad (4)$$

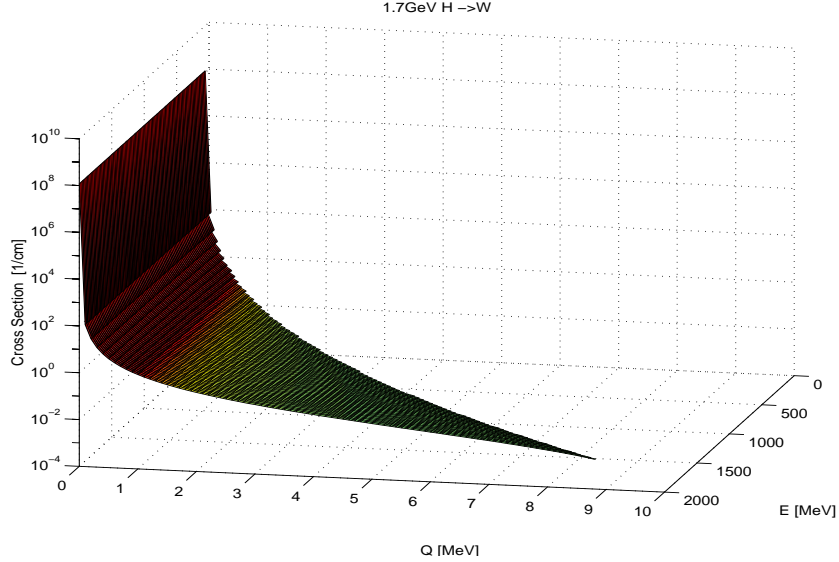


Figure 1: Relativistic Rutherford Cross Section

A plot of the relativistic Rutherford cross section is shown in figure 1. It is evident that small energy transfers by far dominate the energy loss process. Furthermore, because the cross section is extremely large at the small energy transfers, particle energy transfers occur frequently along the ion path.

Because of the frequency of ion-electron collisions and the small energy transfer per collision, the energy loss process is often approximated as a continuous process, commonly referred to as the Continuous Slowing Down (CSD) approximation. The average energy loss or stopping power is obtained by taking the first energy moment of the differential scattering cross section. The stopping power can be expressed as

$$S(E) = \int_{Q_{min}}^{Q_{max}(\beta)} \Sigma(E, Q) Q dQ \text{ (MeV/cm)} \quad (5)$$

where E is the initial particle energy.

Substituting Eq. 2 into Eq. 5 and simplifying yields

$$S(E) = \frac{2\pi Z_p^2 e^4}{m_0 c^2 \beta^2} N Z \left(\ln \frac{Q_{max}(\beta)}{H} - \beta^2 \right) \quad (6)$$

where H is the a lower bound on the allowed energy transfers, which must be much larger than the binding energy of the target electron. This limit on H accounts for contributions from hard collisions only. To approximately account for soft collisions, H is often replaced by the mean excitation-ionization potential, I .

More accurate expressions for $S(E)$ are available, which add semi-empirical corrections to Eq. 6 such as [3]

$$S(E) = \frac{4\pi z^2 e^4 n}{m_0 c^2 \beta^2} \left[\ln \frac{2mc^2 \beta^2}{I(1 - \beta^2)} - \beta^2 - \frac{\sum_i C_i}{Z_M} - \frac{\delta}{2} + \frac{\pi \alpha z \beta}{2} + \frac{z Z_M \alpha^3 F(\beta, Z_M)}{\beta^3} \right] \quad (7)$$

The C_i 's are the electronic shell corrections for the i^{th} electron shell of the target material and represent nonparticipation of the bound electrons in the energy loss process as the ion energy decreases below shell binding energy.

The δ term is a polarization effect that accounts for perturbation of the electron field and reduces the energy lost by the charged particle. The α term and $F(\beta, Z_M)$ are introduced from the second Born approximation and describe

quantum effects [3]. The $F(\beta, Z_M)$ term is only important at low energies while α is important only at ultra-relativistic energies.

The mean excitation-ionization potential is computed from empirical fits or is given by experimental data [3]. Janni lists an empirical formula of

$$I \approx 10.3Z_m(1 - 0.793Z_m^{-2/3}) \quad (eV) \quad Z_m > 34 \quad (8)$$

while Turner [4] lists the formula

$$I \cong \begin{cases} 19.0 & : \quad (eV) \quad Z = 1 \\ 11.2 + 11.7Z_m & : \quad (eV) \quad 2 \leq Z_m \leq 13 \\ 52.8 + 8.7Z_m & : \quad (eV) \quad Z_m > 13 \end{cases} \quad (9)$$

For compounds and mixtures I is computed from the individual elements and the average I is obtained from the Bragg rule [4, 5]. The Bragg rule can be used to yield the average I .

$$\ln(I) = \frac{\sum_i N_i Z_i \ln I_i}{\sum_i Z_i N_i} \quad (10)$$

where i is the index, Z_i is the atomic number, and N_i is the atomic density for the i^{th} material.

2.2 Second Energy Moment

As described previously, high energy ions traverse a the target medium losing energy through frequent and small electronic energy transfers. An average or mean energy loss can be computed to represent the particle's average energy loss in a medium. However, because the electronic interaction of a charged particle with the traversing medium is statistical in nature, not every interaction deposits the same amount of energy. The variation about the mean energy loss is called energy straggling and is responsible for the spreading of the spectra in energy

of an initially monoenergetic beam. A measure of energy straggling is provided by the mean squared energy loss in the target. The expression for the straggling coefficient is

$$T(E) = \int_{Q_{min}}^{Q_{max}(\beta)} \Sigma(E, Q) Q^2 dQ \text{ (MeV}^2/\text{cm)} \quad (11)$$

If the Rutherford differential cross section is substituted into Eq. 11 we get for the straggling coefficient

$$T(E) = \frac{2\pi Z_p^2 e^4}{m_0 c^2 \beta^2} N Z \left[Q_{max} \left(1 - \frac{\beta^2}{2} \right) - Q_{min} \left(1 - \frac{\beta^2 Q_{min}}{2 Q_{max}} \right) \right] \quad (12)$$

where N is the atomic density of the target material. To account for other energy loss fluctuations such as soft collisions, charge exchange, etc., semi-empirical models are frequently employed, such as [6]

$$T(E) = T(E)_{Bohr} \left(\frac{\Omega^2}{\Omega_B^2} \right) \quad (13)$$

where $T(E)_{Bohr}$ is the classical limit of Eq. 12 and is expressed as

$$T(E)_{Bohr} = 4\pi Z_p^2 e^4 N Z \quad (14)$$

and

$$\left(\frac{\Omega^2}{\Omega_B^2} \right)_{Ion} = \gamma^2 \left(\frac{\Omega_{CHU}^2}{\Omega_B^2} \right) + \left(\frac{\Delta \Omega^2}{\Omega_B^2} \right) \quad (15)$$

The γ^2 is the effective charge factor for ions in matter. For solid targets γ^2 is computed from the following relation

$$\gamma^2 = C_3 \left(1 - \exp \left(- \frac{C_4 E}{z_{ion}^{1.5} z_{target}^{0.5}} \right) \right) \quad (16)$$

where C_3 and C_4 are empirical factors obtained from experimental data. The $(\Omega_{CHU}^2/\Omega_B^2)$ factor is computed from

$$\frac{\Omega_{CHU}^2}{\Omega_B^2} = (1 + A_1 E^{A_2} + A_3 E^{A_4})^{-1} \quad (17)$$

where again A_1 , A_2 , A_3 , and A_4 are empirical factors that are fitted to experimental data. For the $(\Delta\Omega^2/\Omega_B^2)$ factor, the relation is

$$\frac{\Delta\Omega^2}{\Omega_B^2} = \frac{B_1 B_3 (1 - e^{-B_4 E})}{(E - B_2)^2 + B_3 (1 - e^{-B_4 E})^2} \quad (18)$$

where B_1 , B_2 , B_3 , and B_4 are empirical factors fitted to experimental data.

Higher energy loss moments can obviously be computed, and these are necessary when describing the energy spectrum near the surface. However, our goal is to develop a simple yet accurate and computationally efficient model of energy straggling suitable for calculating dose distributions, as well as energy spectra at depths not too near the surface. In general, when the incident ions have penetrated the target deep enough to lose approximately 10 percent of it's initial energy the preservation of the mean and the mean squared energy loss is sufficient [7] to accurately characterize the spectrum.

3 Transport Models

The distribution of a beam of ions in energy and space must be known to determine energy spectra, energy deposition, ion deposition, and other physical quantities of interest. Linear transport theory provides an accurate framework for developing a quantitative description of the transport and interaction of ions with amorphous media. In this section, an effective transport equation is presented which accurately preserves the mean and the mean squared energy loss of an initially monoenergetic ion beam, but also incorporates higher energy loss moments approximately. This yields a more robust model than a pure Fokker-Planck model and is suitable for including in multigroup Monte Carlo or deterministic codes.

3.1 Effective Transport Model

Because of the disparate ion-electron mass ratio, there is little or no angular deflection from the electronic interactions, but small angular deflections can result from nuclear interactions. As we are concerned with the electronic interactions only, the small angular deflections are ignored. With this restriction, the transport equation can be expressed as

$$\frac{\partial \Psi}{\partial x} = \int_{Q_{min}}^{Q_{max}} dQ' \Sigma_s(E, Q) \Psi(x, E + Q) - \Sigma_s(E) \Psi(x, E) \quad (19)$$

where x is the distance along the ion path.

To numerically resolve energy transfers associated with these collisions would require an extremely fine mesh in space and energy, which is impractical. However, because the particles interact frequently, the energy loss process can be approximated such that to lowest order only the mean and the mean squared energy-loss moments of the underlying scattering process are preserved. Under

these conditions, the scattering integral can be replaced by a Fokker-Planck approximation given by,

$$\Gamma_{FP}\Psi = \frac{\partial}{\partial E}(S(E)\Psi(x, E)) + \frac{1}{2}\frac{\partial^2}{\partial E^2}(T(E)\Psi(x, E)) \quad (20)$$

where the first energy loss moment coefficient $S(E)$ is expressed in Eq. 5 and the second energy loss moment coefficient $T(E)$ is expressed in Eq. 11. Although higher order terms can be included, the resulting expansion does not yield a robust model [8]. Substitution of Eq. 20 into Eq. 19 leads to

$$\frac{\partial \Psi}{\partial x} = \frac{\partial}{\partial E}(S(E)\Psi(x, E)) + \frac{1}{2}\frac{\partial^2}{\partial E^2}(T(E)\Psi(x, E)) \quad (21)$$

with the incident distribution

$$\Psi(0, E) = \delta(E - E_0) \quad (22)$$

The above transport equation contains a second order energy derivative term that acts as an energy diffusion term and introduces upscatter in energy. While the term represents the physical spreading of the beam, the upscatter effect is not physical. Nevertheless, this model is known to yield accurate spectra in the target interior. A multigroup representation of this model can be obtained using judiciously derived group cross sections. For energy E in group g , the following multigroup transport equation can be shown to be equivalent to the continuous energy Fokker-Planck model in limit of vanishing group width:

$$\begin{aligned} \frac{\partial \Psi(x, E)}{\partial x} - \frac{\partial}{\partial E}(S(x, E)\Psi(x, E)) + (\sigma_{g \rightarrow g+1} + \sigma_{g \rightarrow g-1})\Psi_g^A(x) = \\ \frac{\sigma_{g-1 \rightarrow g}}{\Delta E_g}\Psi_{g-1}^A(x) + \frac{\sigma_{g+1 \rightarrow g}}{\Delta E_g}\Psi_{g+1}^A(x) \end{aligned} \quad (23)$$

Where $E_{g+\frac{1}{2}} \leq E \leq E_{g-\frac{1}{2}}$, $g = 1, 2, 3 \dots N_G$. The cross section represents the combined effect of many statistical collision events that result in small energy

transfers. Thus the cross section should only describe scattering to adjacent groups for a energy group exceeding the actual mean energy loss per collision. The particles are never allowed to straggle above the their initial energy and exit the system if they cross the cutoff or minimum energy. The cross sections are then defined such that the mean squared energy loss in scattering out of group g is preserved, i.e.

$$\sigma_{g \rightarrow g'} (E_g - E_{g+1})^2 = \frac{T_g}{2} \quad \text{for } g' = g + 1$$

$$\sigma_{g \rightarrow g'} = 0 \quad \text{for } g' \neq g + 1 \quad (24)$$

$$(25)$$

and

$$\sigma_{g \rightarrow g'} (E_g - E_{g-1})^2 = \frac{T_g}{2} \quad \text{for } g' = g - 1$$

$$\sigma_{g \rightarrow g'} = 0 \quad \text{for } g' \neq g - 1 \quad (26)$$

$$(27)$$

For the first energy group the cross section is twice that of the downscatter piece and the upscatter piece is defined to be zero. Thus no upscatter can occur above the initial particle energy, E_0 . The above multigroup model suffers from the same short coming of the Fokker-Planck model, namely the presence of upscatter. Not only is this feature unphysical (although the effect is small) it introduces unnecessary algorithmic complexities when a deterministic numerical solution of Eq. 23 is attempted. To circumvent this difficulty we propose the following simpler, strictly downscatter model:

$$\frac{\partial \Psi(x, E)}{\partial x} - \frac{\partial}{\partial E} (S(x, E) \Psi(x, E)) + \sigma_{g \rightarrow g+1} \Psi_g^A(x) = \frac{\sigma_{g-1 \rightarrow g}}{\Delta E_g} \Psi_{g-1}^A(x) \quad (28)$$

The cross section for this model is given by

$$\begin{aligned}\sigma_{g \rightarrow g'} (E_g - E_{g+1})^2 &= T_g & g' = g + 1 \\ \sigma_{g \rightarrow g'} &= 0 & g' \neq g + 1\end{aligned}\tag{29}$$

where now the mean square energy loss is entirely preserved by scattering to the adjacent lower energy group. However, by virtue of the nonsymmetric process, an additional, spurious, mean energy loss associated with $\sigma_{g \rightarrow g+1}$ is introduced. The stopping power associated with this extra energy loss may be expressed as

$$S_g^* = \sigma_{g \rightarrow g+1} (E_g - E_{g+1})\tag{30}$$

and an effective group stopping power defined by

$$\overline{S}_g = S_g - S_g^*\tag{31}$$

to ensure preservation of the physical mean energy loss. Our multigroup straggling model is tested in the next section using a Monte Carlo implementation.

4 Single Event Monte Carlo and Multigroup Monte Carlo Simulations

In this chapter the results of multigroup Monte Carlo upscatter and downscatter models are compared against a single event Monte Carlo code that simulates individual ion-electron interactions using the relativistic Rutherford cross section. The latter provides a benchmark for the multigroup straggling model proposed earlier. The total scattering cross section is on the order of 10^4 cm^{-1} which results in small mean free paths and makes the single event Monte Carlo method very time consuming to run. The multigroup model cross sections, on the other hand, are on the order of 10^{-1} cm^{-1} and thus are relatively quick to run.

For the comparisons, the two problems of interest are a 1700 MeV beam of protons on a tungsten target and a 3.75 MeV beam of alpha particles on an aluminum target. The 1700 MeV proton beam problem is representative of recent accelerator driven nuclear applications [9], and the 3.75 MeV alpha particle beam problem is a simulation of alpha particles resulting from a fusion reaction impacting on an aluminum barrier.

4.1 Single Event Monte Carlo Code

In the single event Monte Carlo simulation, the distance to collision is sampled from an exponential distribution with mean free path given by the total scattering cross section, and the energy loss in a collision is sampled from the normalized differential cross section. The Rutherford cross section may be expressed as

$$\sigma(E, Q) = \sigma(E)P(Q), \quad Q_{min} \leq Q \leq Q_{max} \quad (32)$$

where

$$\sigma(E) = \int_{Q_{min}}^{Q_{max}} \sigma(E, Q) dQ \quad (33)$$

and $P(Q)$ is a normalized distribution given by

$$P(Q) = \frac{\sigma(E, Q)}{\sigma(E)} \quad (34)$$

The Rutherford cross section is

$$\sigma(E, Q)dQ = \frac{0.1536 Z_1^2 Z_2 \rho}{A_2 \beta^2 Q^2} \left(1 - \beta^2 \frac{Q}{Q_{max}} \right) \quad (35)$$

All ions are started at an initial energy E_0 and at distance $x = 0$. A random number ξ is generated and the distance to collision is determined by the expression

$$\Delta x_{dc} = \frac{-\log(\xi)}{\sigma(E)} \quad (36)$$

This distance is compared against the distance to the end of the slab. If the distance to collision is smaller than the distance to the end of the slab, the particle is moved forward by the increment Δx_{dc} , and the energy loss is sampled. If the distance to the end of the slab is smaller than the distance to collision, the particle is moved to the end of the slab and the ion energy is scored.

The amount of energy lost can be obtained by generating a new random number ξ , and setting that number to a cumulative distribution function of the cross section. This is expressed as

$$\xi = \int_0^Q P(Q') dQ' \quad (37)$$

where Q is the energy transfered in the collision. The evaluation of the cumulative distribution function results in a nonlinear expression of Q . To get Q , a fixed point iteration method is applied to Eq. 37.

After the energy lost from the collision is subtracted from the particle's current energy, a new distance to collision is computed based upon the new

energy. The process is repeated until the particle reaches the end of the slab. The particle distance and energy is the scored, and then another particle can be simulated. To minimize statistical error, typically one to ten million particle histories are simulated.

4.2 Multigroup Monte Carlo Codes

The multigroup Monte Carlo methods use a divided energy domain of contiguous elements called groups. By allowing collision events to be averaged over a group, a significant gain in the speed of the computation occurs. For the multigroup Monte Carlo methods the individual electronic collisions are replaced by transitions to adjacent groups with probabilities determined by group averaged cross sections. The mean energy loss given by the continuous slowing down representation is simulated exactly between collisions, so that the method is actually a hybrid deterministic-Monte Carlo model.

The particles are initially started at $x = 0$ and randomly distributed within the first energy group which is expressed as

$$E_0 = E_{\frac{3}{2}} - \xi \delta E_1$$

where ξ is a random number. Once initially assigned, the particle travels through the slab. A distance to collision is computed from the formula

$$\Delta x_{dc} = \frac{-\log(\xi)}{\sigma_{total,g}} \quad (38)$$

for group g and where $\sigma_{total,g}$ for the upscatter model is

$$\sigma_{total,g} = \sigma_{g \rightarrow g+1} + \sigma_{g \rightarrow g-1} \quad (39)$$

and for the downscatter model is

$$\sigma_{total,g} = \sigma_{g \rightarrow g+1} \quad (40)$$

The distance to collision is compared to the distance to the bottom energy group boundary and to the distance to the end of the slab. If either the energy boundary or the slab boundary is smaller than the distance to collision, then the particle is moved by that distance and loses energy according to the current group stopping power. The energy loss is expressed as

$$E_{current} = E_{previous} - S_g \Delta x_{collisiontype}$$

If the distance to collision is smaller than the distance to bottom energy group boundary or distance to end of slab, the particle is collided and either gains or loses energy by ΔE_g for upscatter or just loses energy by ΔE_g for downscatter. The calculation continues until the particle exits the slab. Then the particle energy and distance are scored and the next particle can be simulated. Again, one to ten million histories are simulated in order to accumulate adequate statistics.

4.3 Results

For the single event and the multigroup Monte Carlo methods, the exiting particle position and energy are written to a file and then binned based on the group structure. Results have been obtained for the 1700 MeV protons on tungsten at depths of 2, 5, 10, 20, 43, 65, and 85 cm. The incident proton for the 1700 MeV protons on tungsten problem using the Rutherford cross section has a range of 130cm, so that 43, 65 and 85cm distances represent one-third, one-half, and two-thirds range respectively. We begin by examining proton spectra in tungsten at depths of 10, 20, 43, 65, and 85cm.

For these cases, the energy group widths are 8.54 MeV. A much wider group width can be applied because the spectra has spread sufficiently for this depth. Overall both the upscatter and downscatter Monte Carlo methods capture the spectra behavior very well. The 10cm upscatter case agrees quite well with the

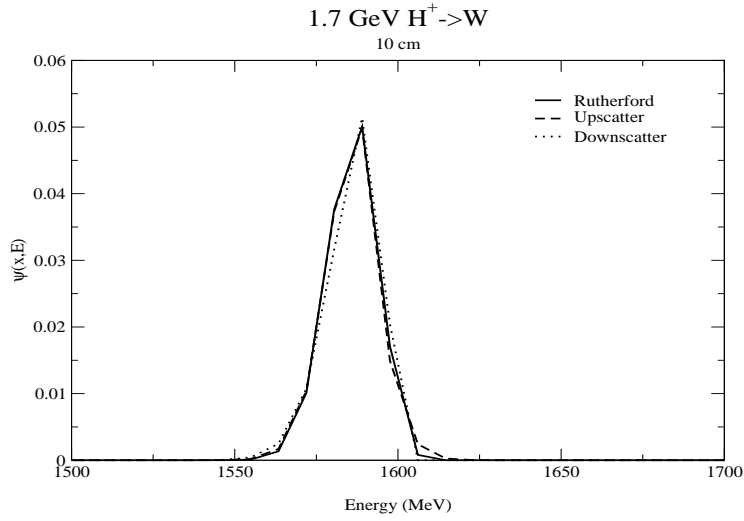


Figure 2: Spectra at 10cm for Protons on Tungsten

single event Monte Carlo but then the 20 and 43 cm cases have the upscatter model slightly overshooting the peak. These effects are due to the binning of the Monte Carlo data, and refined energy group structures and more particles would smooth these effects out.

However, the downscatter model underestimates the spectra at the high energies and slightly overestimates at the lower energy tail. The differences can be attributed to an overestimate of higher energy loss moments, particularly the mean cubed, by the downscatter model, which results in a more skewed spectrum. The upscatter model, which has no mean cubed energy loss, shows better results than the downscatter.

For the 2cm and 5cm cases a finer energy group width of 0.5 MeV is needed so as to accurately resolve the spectrum. The upscatter and downscatter Monte Carlo models clearly do not agree as well as the cases deep within the slab. The explanation for the disagreement is that higher moments such as the mean cubed become important near the surface of the slab. The higher moments effects fall

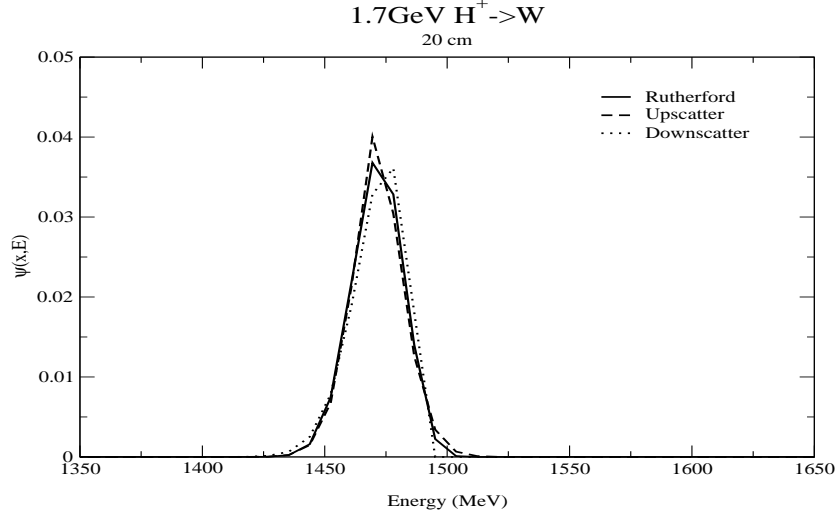


Figure 3: Spectra at 20cm for Protons on Tungsten

rapidly with decreasing energy. Thus near the surface and at high energies where higher moments are important the spreading is not accurately captured by the cross section model because the cross section model only captures the mean squared.

For alpha particles on aluminum the results obtained were at 0.0001, 0.00025, 0.0005, 0.001, 0.0015, and 0.002cm. The total range for the alpha particles in this problem was 0.003cm. For the 0.0001 and 0.00025cm cases, $\Delta E_g = 0.00375$ MeV was necessary to obtain smooth spectra. We note that in all cases the multigroup results, rigorously preserving only the mean and mean-square energy losses, are in excellent agreement with the exact single event results. The reason is that at these low energies, the mean energy loss dominates and the mean-square moment is significantly larger than the higher moments.

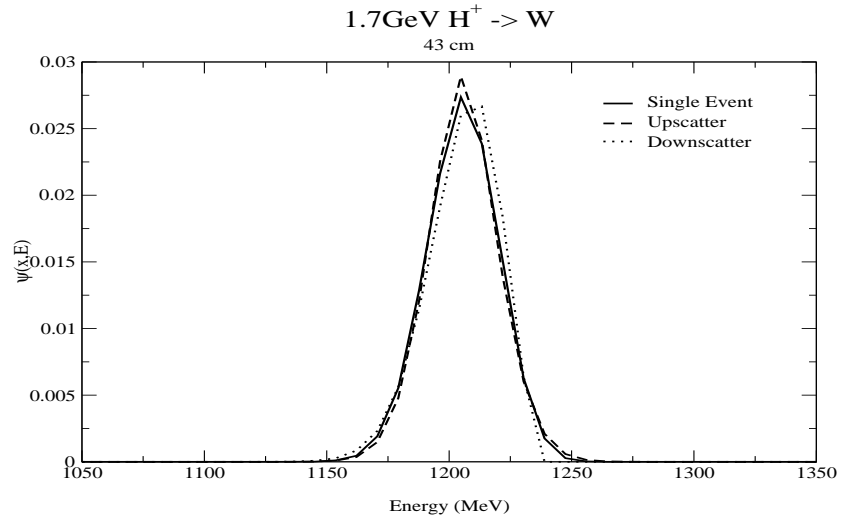


Figure 4: Spectra at 43cm for Protons on Tungsten

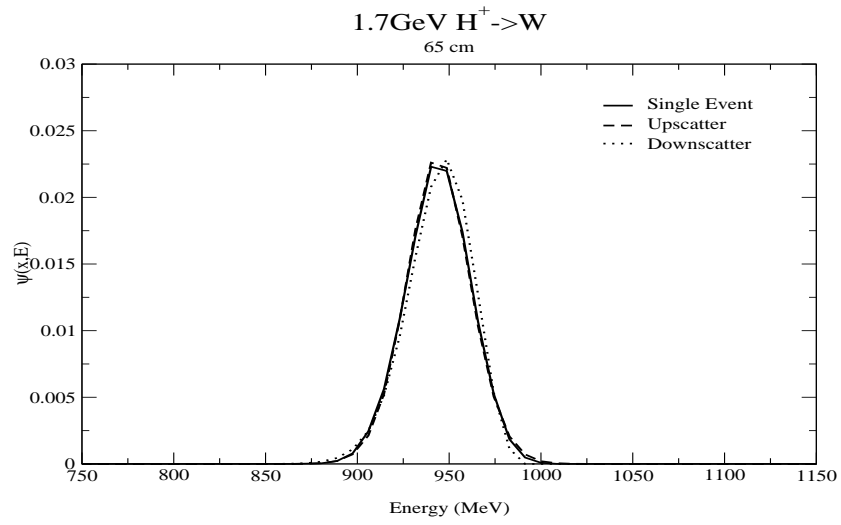


Figure 5: Spectra at 65cm for Protons on Tungsten

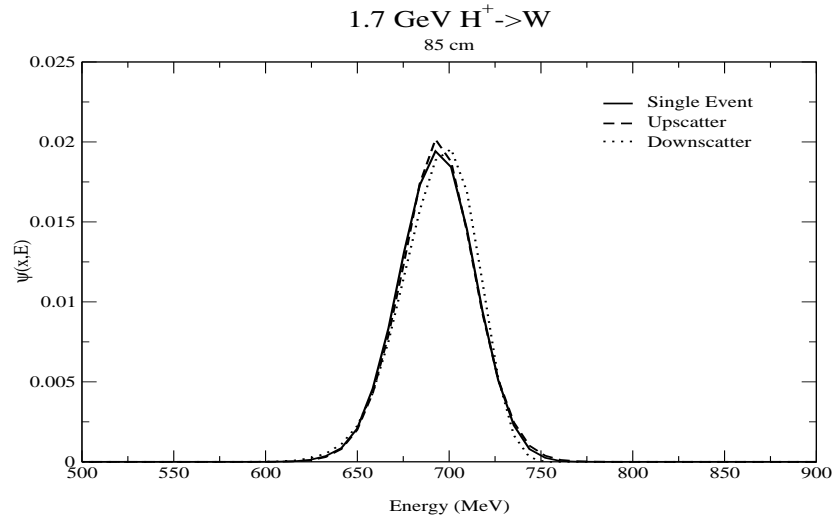


Figure 6: Spectra at 85cm for Protons on Tungsten

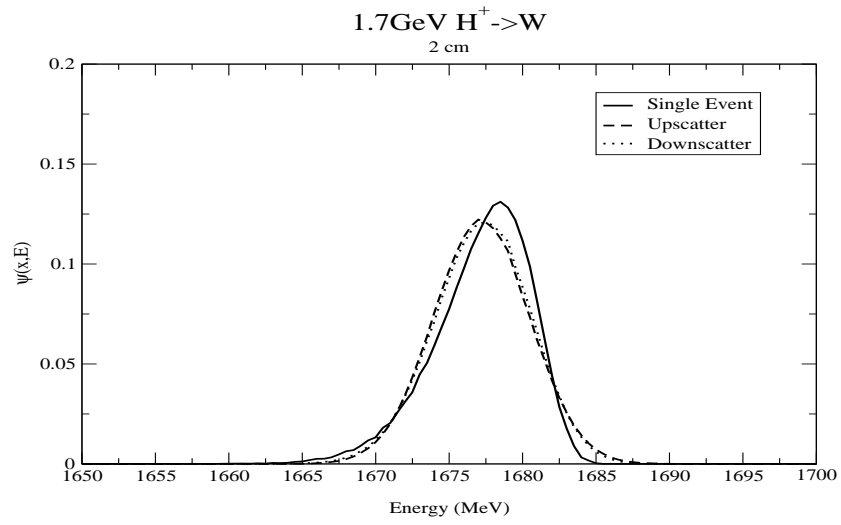


Figure 7: Spectra at 2cm for Protons on Tungsten

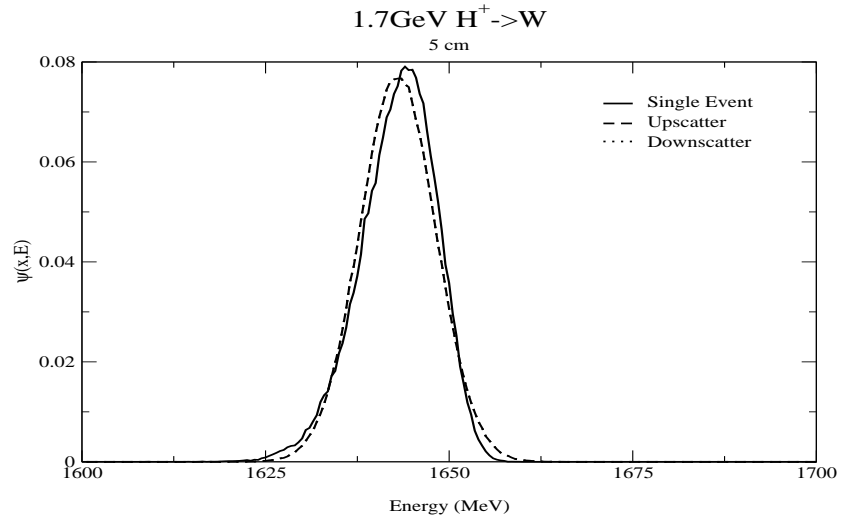


Figure 8: Spectra at 5cm for Protons on Tungsten

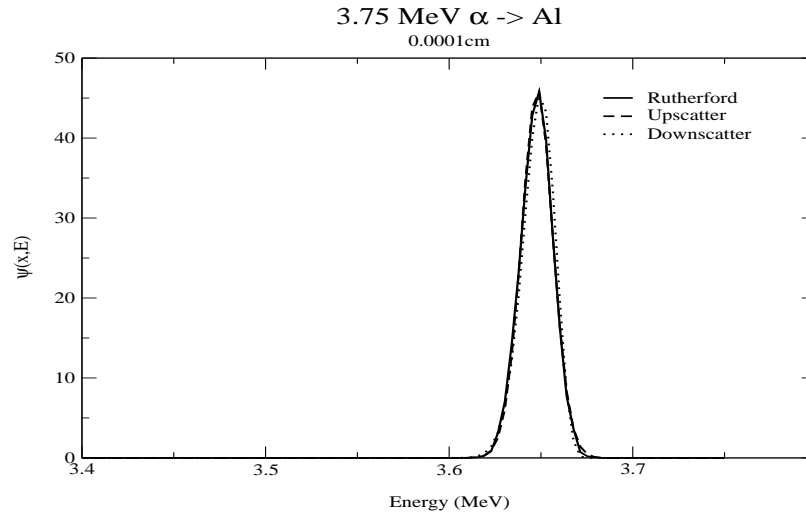


Figure 9: Spectra at 0.0001cm for alpha particles on aluminum

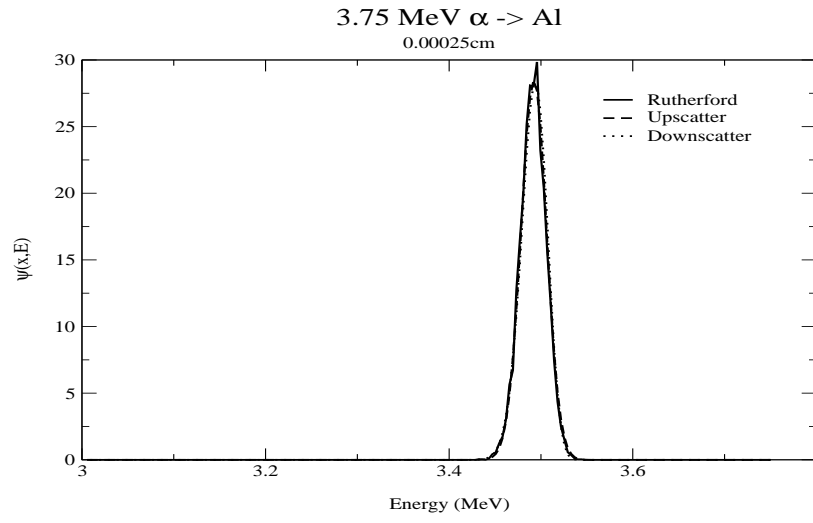


Figure 10: Spectra at 0.00025cm for alpha particles on aluminum

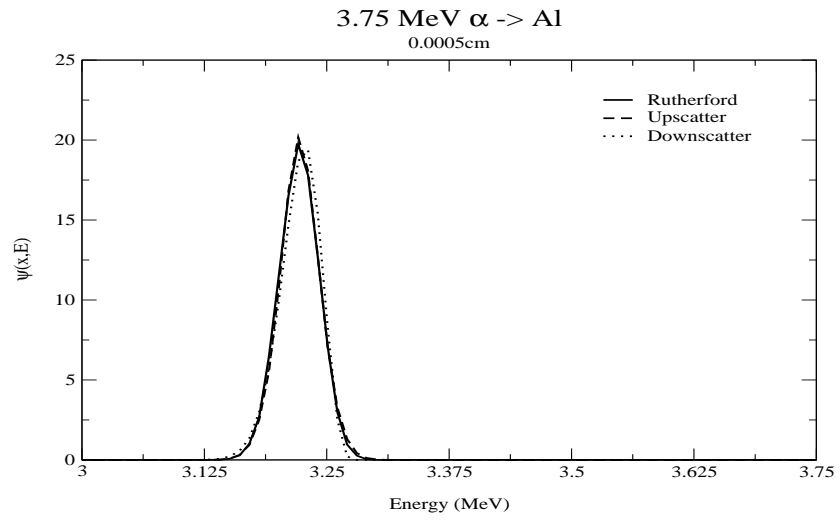


Figure 11: Spectra at 0.0005cm for alpha particles on aluminum

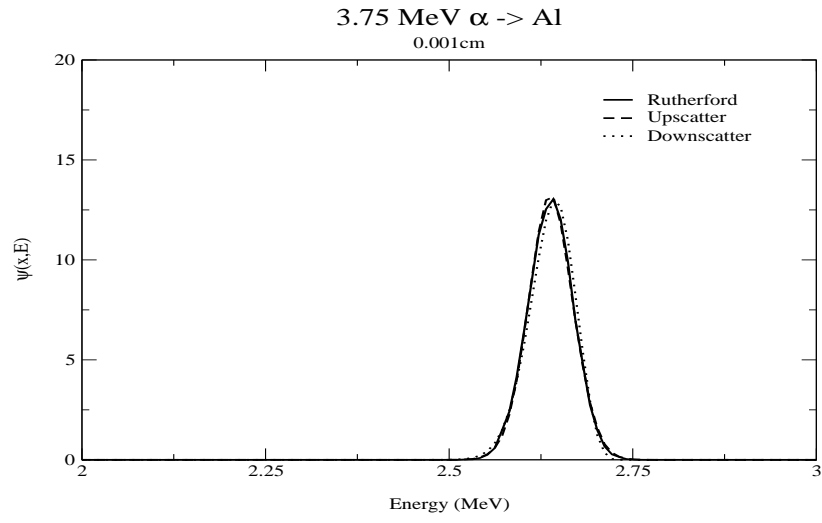


Figure 12: Spectra at 0.001cm for alpha particles on aluminum

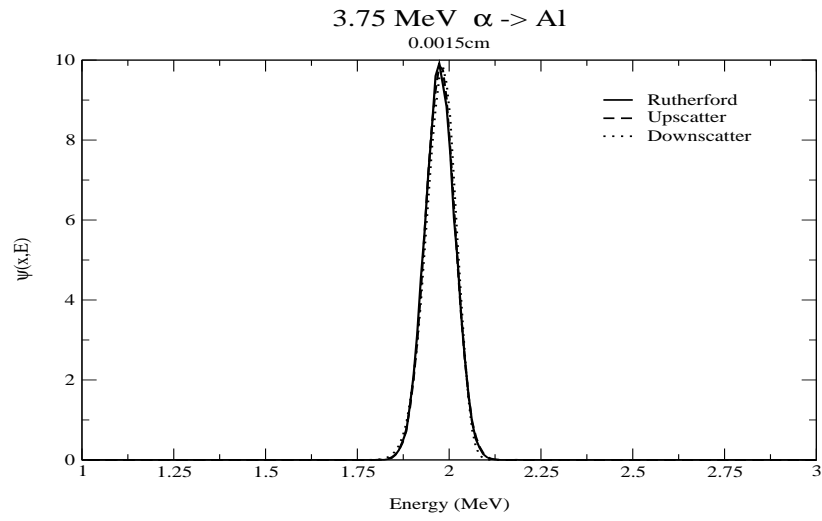


Figure 13: Spectra at 0.0015cm for alpha particles on aluminum

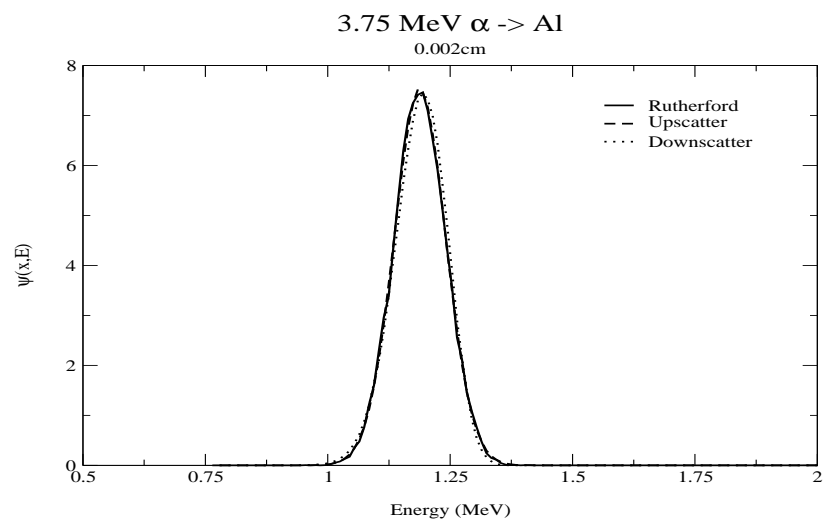


Figure 14: Spectra at 0.002cm for alpha particles on aluminum

5 Arbitrary Order Linear Discontinuous Finite Element Methods

In this and the following sections we consider deterministic numerical solution of the effective transport equations introduced and examined in the previous chapters. In particular we use the Galerkin finite element method in space and energy to construct numerical schemes that have arbitrary orders of accuracy. Low order finite element methods have been used extensively with great success for neutral particle transport where collisions are well defined discrete interactions and distributions are broad. However, for charged particles, which essentially slow down continuously, the energy and angular distributions relax slowly and require higher order numerical representations. This is particularly true for monoenergetic incidence and hence is relevant to the considerations of this report.

Two families of approximating trial functions on a space-energy grid are considered. In the present and next section, a linear family of arbitrary polynomial degree trial functions is first investigated with applications to the upscatter and strictly downscatter straggling models. Numerical results are compared against the multigroup Monte Carlo results of the previous chapter to assess accuracy and robustness. Then in the following two sections a novel non-linear family of trial functions is proposed and tested. This is a computationally more demanding approach but has great promise because the scheme is inherently positive and monotone.

5.1 Finite Element Background

The general finite element approach is a popular method for solving different challenging problems in science and engineering, and is well documented in the literature. [10, 11, 12, 13, 14] Here we present a brief and general background

and then look at specific problems of interest to us.

The finite element technique seeks to represent the solution u to an operator equation represented by

$$L(u) = f$$

where the operator $L()$ is a linear operator and where f is a function of the independent variables. This form of the equation is sometimes called the “strong form”.

The finite element method starts by discretizing the domain into pieces or elements. The discretization is done so that the solution can be represented over the smaller elements rather than the whole domain.

Next a basis set is chosen to approximate u . The approximation is expressed as

$$u \approx v = \sum_{j=1}^N U_j B_j$$

where B_j are the trial basis functions and U_j are the unknown coefficients. In the effective transport equation B_j will be a function of space and energy and U_j be the associated coefficients. The approximation of u is not exact and when v is substituted into the linear operator an error or residual results which, may be expressed as

$$R(v) = L(v) - f \neq 0$$

The residual can be minimized by multiplying the residual by a weight function and then integrating the resulting product over each element.

$$\langle \omega_j | L(u) - f \rangle = 0, j = 1, \dots, N$$

where ω_j are suitable weight functions. If L is a differential operator then integrating by parts allows continuity conditions on the trial functions to be relaxed. The resulting form is called the “weak form”.

The result is a system of equations that can be solved for the approximation coefficients U_j . If the weights and the approximation of u are constructed from the same basis functions, the method is referred to as the Galerkin finite element method. Other bases can be chosen such that the weights and the approximated solution are different. (this will be the case in our second method using nonlinear trial functions.) The weak form allows the trial functions to be discontinuous at the inflow boundary of each element. The extra freedom yields higher accuracy, greater robustness, and although strictly positive solutions are not guaranteed, any negativities are strongly damped as a result of allowing discontinuities in the trial functions.

The final step is to solve the linear system of algebraic equations for the unknown coefficients that results from the residual minimization over each element.

We begin by discretizing the space and energy domain into elements, with G energy groups and K spatial cells such that $E_{g-\frac{1}{2}} > E \geq E_{g+\frac{1}{2}}$ and $x_{k-\frac{1}{2}} < x \leq x_{k+\frac{1}{2}}$. For each element the flux is approximated by a $A \times B$ degree polynomial where A is the maximum order of the spatial expansion and B is the maximum order of the energy expansion. The constant or flat polynomial is used to ensure particle balance and the first energy moment for energy balance. With the exception of these two requirements the polynomial representation minimized over each element can be constructed to whatever order the user wants with any number or cross terms. The polynomials do not have to be made up of complete sets with cross terms. Any combination that contains the flat and first order in energy is permissible. Again the values of A and B are arbitrary assuming sufficient computer resources can be obtained. In particular, we choose Legendre polynomials as trial functions and exploit their

orthogonality to greatly simplify the construction of the linear system. Legendre polynomials may be defined by Rodrigues's formula [15]

$$P_n(z) = \frac{1}{2^n n!} \frac{d^n}{dz^n} [(z^2 - 1)^n] \quad (41)$$

The orthogonality of the Legendre polynomials over $(-1,1)$ may be expressed as

$$\int_{-1}^1 P_n(z) P_{n'}(z) dz = \begin{cases} \frac{2}{2n+1} & n = n' \\ 0 & n \neq n' \end{cases} \quad (42)$$

For representation on the grid element $(x_{k-\frac{1}{2}}, x_{k+\frac{1}{2}}) \times (E_{g+\frac{1}{2}}, E_{g-\frac{1}{2}})$ we use shifted Legendre polynomials, expressed as

$$p_a^k(x) = \begin{cases} P_a \left[\frac{2}{\Delta x_k} (x - x_k) \right] & : \text{ for } x_{k-\frac{1}{2}} < x \leq x_{k+\frac{1}{2}} \\ 0 & : \text{ otherwise} \end{cases} \quad (43)$$

$$p_b^g(E) = \begin{cases} P_b \left[\frac{2}{\Delta E_g} (E - E_g) \right] & : \text{ for } E_{g+\frac{1}{2}} \leq E < E_{g-\frac{1}{2}} \\ 0 & : \text{ otherwise} \end{cases} \quad (44)$$

The trial function for the space-energy flux is then expressed as

$$\Psi_n(x, E) \approx \sum_{a=0}^A \sum_{b=0}^B p_a^k(x) p_b^g(E) \Psi_{k,g}^{a,b} \quad (45)$$

where g is the energy group index, k is the spatial cell index, and a and b are the Legendre polynomial indices for space and energy moments. In following the Galerkin procedure, we take for the weight functions in cell k' and group g'

$$p_{a'}^{k'}(x) p_{b'}^{g'}(E), a' = 0, 1, 2, \dots, N, b' = 0, 1, 2, \dots, B \quad (46)$$

This choice of weight functions ensures at a minimum the preservation of particle number and energy, important constraints for the class of problems

of interest here. The trial functions are further allowed to be discontinuous at inflow boundaries in space and energy as depicted in fig. 15 This provides varying solutions while minimizing over- and under-shoot and enhancing overall robustness.

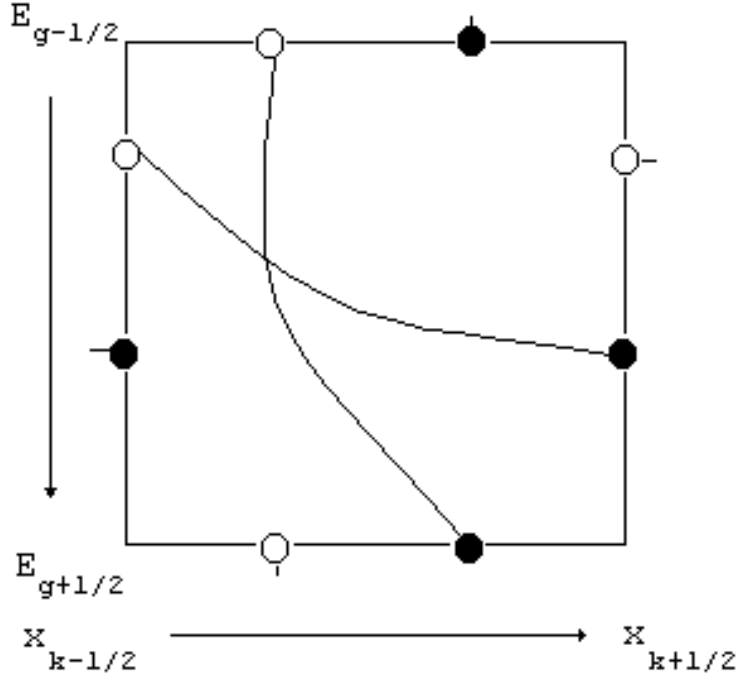


Figure 15: Graphic of finite element at x_i and E_g

5.2 Linear Family of Arbitrary Degree

Polynomial Discontinuous Finite Element Solutions

We proceed with applying the method outlined above to the effective transport equations. In particular we demonstrate the method on the upscatter model because the downscatter model easily follows as a special case. Taking the inner product with the weight functions leads to

$$\langle \omega_{a',b'} | L(\Psi) - Q \rangle = 0, a' = 0 \cdots A, b' = 0 \cdots B$$

where

$$L = \frac{\partial}{\partial x} - \frac{\partial}{\partial E} S(x, E) + \sigma_{g \rightarrow g+1} []^A + \sigma_{g \rightarrow g-1} []^A \quad (47)$$

and

$$Q = \int_{E_{g-\frac{3}{2}}}^{E_{g-\frac{1}{2}}} dE' \sigma_{g-1} \Psi^A(x, E') + \int_{E_{g+\frac{1}{2}}}^{E_{g+\frac{3}{2}}} dE' \sigma_{g+1} \Psi^A(x, E') \quad (48)$$

and where a' and b' are the order indices for the weight function ω . The upscatter finite element model has an unknown source term from particles that scatter up from adjacent groups and introduces iterations over the entire element grid which are indexed by j . For the downscatter model no particles are scattered up from the group below, and thus no iterations are necessary, making it computationally more efficient than the upscatter model. Introducing the terms explicitly, the weighted residual becomes

$$\begin{aligned} & \int_g \Psi^{j+1}(x, E) \big|_{k+\frac{1}{2}} \omega(x, E) \big|_{k+\frac{1}{2}} dE - \int_g \Psi^{j+1}(x, E) \big|_{k-\frac{1}{2}} \omega(x, E) \big|_{k-\frac{1}{2}} dE \\ & \int_k \int_g \Psi^{j+1}(x, E) \frac{\partial \omega(x, E)}{\partial x} dE dx - \int_k (S(x, E) \Psi^{j+1}(x, E)) \big|_{g-\frac{1}{2}} \omega(x, E) \big|_{g-\frac{1}{2}} dx \\ & + \int_k (S(x, E) \Psi(x, E)^{j+1}) \big|_{g+\frac{1}{2}} \omega(x, E) \big|_{g+\frac{1}{2}} dx + \int_k \int_g S(x, E) \Psi^{j+1}(x, E) \frac{\partial \omega(x, E)}{\partial E} dE dx \\ & \int_k \int_{g+1} \sigma_{g+1} \Psi^{A,j}(x, E) \int_g \omega(x, E) dE dx = \\ & \int_{g-1} \int_k \frac{\sigma_{g-1}}{\Delta E_g} \Psi^{A,j+1}(x, E') \int_g \omega(x, E) dx dE \end{aligned} \quad (49)$$

Next, we integrate the streaming terms in space and energy and introduce the discontinuity by setting the inflow current to the exiting flow from the previous element. For every element g, k the resulting weak form is given by

$$\begin{aligned} & \int_g \Psi^{j+1}(x, E) \big|_{k+\frac{1}{2}} \omega(x, E) \big|_{k+\frac{1}{2}} dE - \int_g \Psi^{j+1}(x, E) \big|_{k-1} \omega(x, E) \big|_{k-\frac{1}{2}} dE \\ & \int_k \int_g \Psi^{j+1}(x, E) \frac{\partial \omega(x, E)}{\partial x} dE dx - \int_k (S(x, E) \Psi^{j+1}(x, E)) \big|_{g-1} \omega(x, E) \big|_{g-\frac{1}{2}} dx \\ & + \int_k (S(x, E) \Psi(x, E)^{j+1}) \big|_{g+\frac{1}{2}} \omega(x, E) \big|_{g+\frac{1}{2}} dx + \int_k \int_g S(x, E) \Psi^{j+1}(x, E) \frac{\partial \omega(x, E)}{\partial E} dE dx \end{aligned}$$

$$\begin{aligned}
& \int_k \int_g \sigma_{g \rightarrow g'}(x, E) \Psi^{A, j+1}(x, E) \omega(x, E) dE dx = \\
& \int_{g-1} \int_k dE' \frac{\sigma_{g-1}}{\Delta E_g} \Psi^{A, j}(x, E') \int_g \omega(x, E) dx dE
\end{aligned} \tag{50}$$

Introducing the weight functions explicitly and simplifying gives, after much algebra,

$$\begin{aligned}
& \left(\frac{\Delta E_g}{2} \right) \frac{2}{2a'+1} \sum_{b=0}^B \left(1 - \gamma_b \frac{2}{2b+1} \right) \Psi_{a', b}^{j+1, g, k} \\
& + S_g \left(\frac{\Delta x_k}{2} \right) \frac{2}{2b'+1} \sum_{a=0}^A \left((-1)^{a+a'} + \gamma_a \frac{2}{2a+1} \right) \Psi_{a, b'}^{j+1, g, k} \\
& + \sigma_{g \rightarrow g'} \left(\frac{\Delta x_k}{2} \right) \frac{2}{2b'+1} \Delta E_g \Psi_{0, b'}^{j+1, g, k} = \\
& \Delta E_{g-1} \Delta E_g \sigma_{g-1} \frac{\Delta x_k}{2} \frac{2}{2b'+1} \Psi_{0, b'}^{j, g-1, k} \\
& + S_{g-1} k \sum_{a=0}^A (-1)^a \left(\frac{\Delta x_k}{2} \right) \frac{2}{2b'+1} \Psi_{n, a, b'}^{j+1, g-1, k} + \mu_n \sum_{b=0}^B \left(\frac{\Delta E_g}{2} \right) \frac{2}{2a'+1} \Psi_{n, a', b}^{j+1, g, k-1} (-1)^{b'}
\end{aligned} \tag{51}$$

where the γ_b and γ_a are coefficients resulting from the expansion of the derivative of the Legendre polynomial in terms of Legendre polynomials.

Defining $\Psi_{k, g}^{j+1}$ as the vector of unknowns, the above systems can be expressed in compact matrix-vector notation as

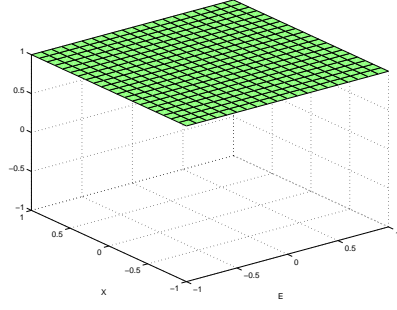
$$\mathcal{A} \Psi_{k, g}^{j+1} = \mathcal{B} \Psi_{n, k-1, g}^j + \mathcal{C} \Psi_{k, g-1}^j + \mathcal{Q}_{k, g}^j \tag{52}$$

where the order of the matrix \mathcal{A} is $(A+1) \times (B+1)$. The maximum order of the matrix is fixed a priori and the algorithm proceeds by marching across the spatial cell row and then down in energy, locally inverting a $(A+1) \times (B+1)$ system in each 2D element (k, g) .

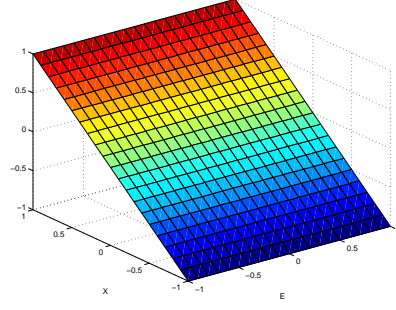
The outer iterations (on $\Psi_{g+1, k}^{0,0}$) for the upscatter model are converged to a preset tolerance according to the L_2 norm given by

$$\epsilon > \sqrt{\frac{\sum_{g=1}^{N_g} \sum_{k=1}^{N_k} \left(\Psi_{g, k}^{j, 0, 0} - \Psi_{g, k}^{j+1, 0, 0} \right)^2}{N_g N_k}} \tag{53}$$

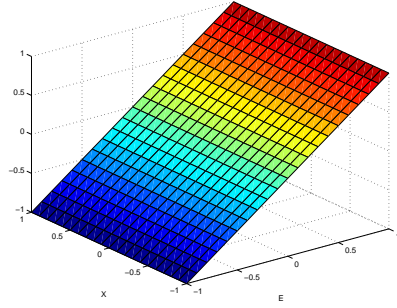
Table 1: Graphical Representation of Legendre Moments



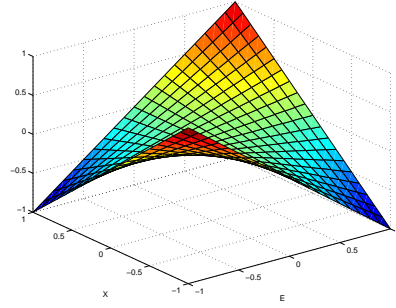
a. $P_0(z_E)P_0(z_x)$



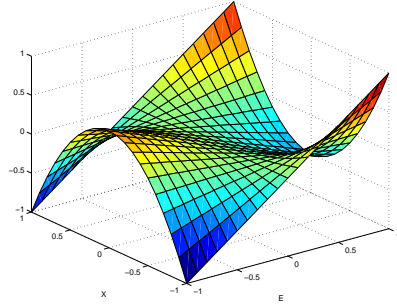
b. $P_0(z_E)P_1(z_x)$



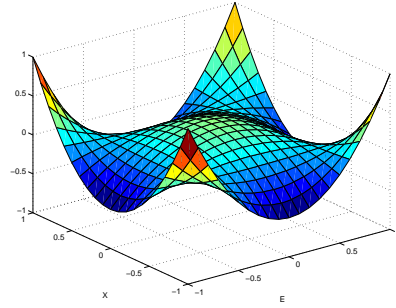
c. $P_1(z_E)P_0(z_x)$



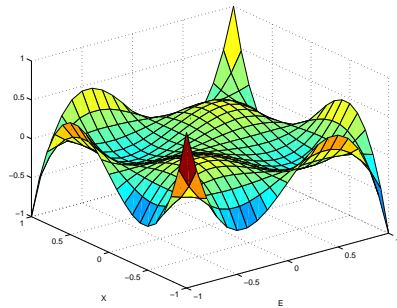
d. $P_1(z_E)P_1(z_x)$



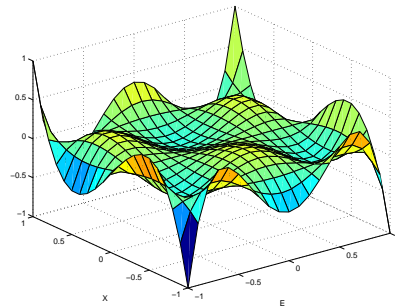
e. $P_1(z_E)P_2(z_x)$



f. $P_2(z_E)P_2(z_x)$



g. $P_3(z_E)P_3(z_x)$



h. $P_4(z_E)P_3(z_x)$

6 Numerical Results for Linear Family Methods

The multigroup Monte Carlo implementation of our straggling model clearly demonstrated the accuracy of the model at a sufficient depth. Excellent agreement was realized for 1.7GeV protons on tungsten and 3.75MeV alpha particles on aluminum and similar agreement is expected with other ion-target combinations. In this section we consider numerical results obtained using the linear family of arbitrary polynomial discontinuous finite element method described in the previous section. The finite element approach yields results that are quick to obtain and gives fitted polynomials over each element, allowing quantities such as spectra, dose, and ion deposition to be computed.

The convergence with number of groups, number of spatial cells, and convergence in polynomial order are compared against the multigroup Monte Carlo results. The results in this section were calculated with the Rutherford stopping power given in Eq. 6 and the Rutherford energy straggling coefficient given by Eq. 12. All upscatter finite element results are converged to a tolerance of 1.0×10^{-8} , with uniform spatial and energy cells.[16].

6.1 Convergence of the Space Energy Mesh

To obtain an accurate solution the finite element method must minimize the error of a polynomial fit over elements. The elements must divide the domain such that an accurate representation can be obtained but yet the division must not be extremely fine where little is gained for the extra division. Furthermore, the cost of obtaining the polynomial fit increases with increasing order, spatial discretization, and energy discretization. Convergence studies of the space and energy discretization can help determine if the approximated polynomial fit is representing the desired solution or if the element structure is too crude to do so.

For the convergence study a low order polynomial method, the bi-linear discontinuous (BLD), and a higher order polynomial method, the quadratic discontinuous (QD), were selected to be examined. Results from higher order trial functions will also be presented. The spectra are examined at the one-third range position of 43.0cm, where our straggling model is known to be accurate but the distributions are peaked enough for high order methods to make a difference. The different energy group and spatial step structures are given in table 2.

Table 2: Table of number of energy groups to energy group widths and number of spacial cells to spacial cell width

Number of Groups	ΔE_g	Number of Spacial Cells	Δx_k
50	33.998 MeV	130	1 cm
100	16.999 MeV	260	0.5 cm
200	8.5 MeV	520	0.25 cm
400	4.25 MeV	1040	0.125 cm
800	2.125 MeV	-	-

As the group structure changes so does the energy straggling cross section and the Monte Carlo multigroup bin structure. To account for the changes due to group structure, results from the finite element results must be plotted against the appropriate Monte Carlo multigroup result. The energy group refinement is shown in figures 16, 17, 18, and 19. Each group refinement case had a spatial step size of 0.1cm.

In figure 16 and 18 we note that the upscatter and downscatter BLD results are not fully converged even at the extremely refined group structure of 800 groups. On the other hand, figure 17 and 19 show that the QD method converges for 200 energy groups. This is an important result that has not been demonstrated before - the widely used LD and BLD finite element representations that are so extensively employed in neutral particle transport prove inadequate for

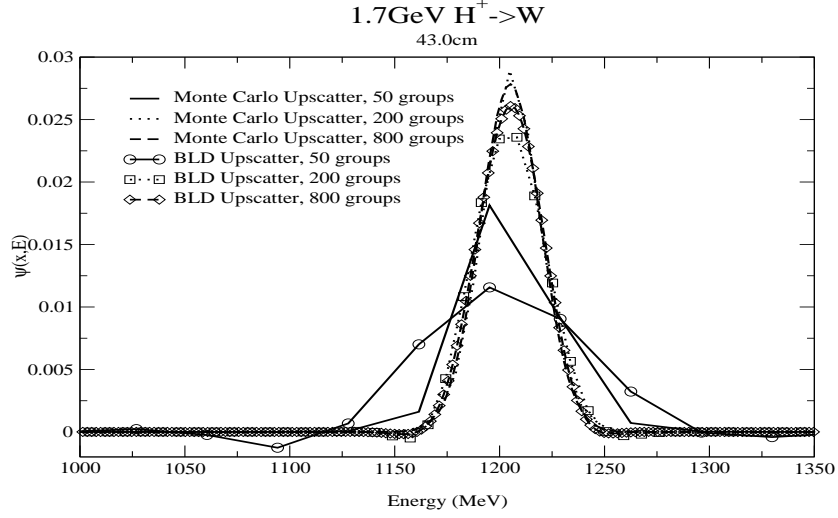


Figure 16: Bi-linear discontinuous upscatter finite element group convergence for protons on tungsten at 43.0cm

charged particle transport. Note also that the negative oscillations in the tails are highly damped in all cases.

For the convergence in space all results are computed with a $\Delta E_g = 8.5$ MeV which is near the maximum energy transfer computed for the Rutherford cross section. The quadratic discontinuous finite element method shown in figures 22 and 23 converge in space for 130 spacial steps. The BLD finite element methods shown in figures 20 and 21 converge in space at 260 steps but need much greater refinement in energy to approach the Monte Carlo multigroup results. Furthermore, both the BLD and QD finite element methods show a dissipation of the negative oscillations with decreasing spacial step size.

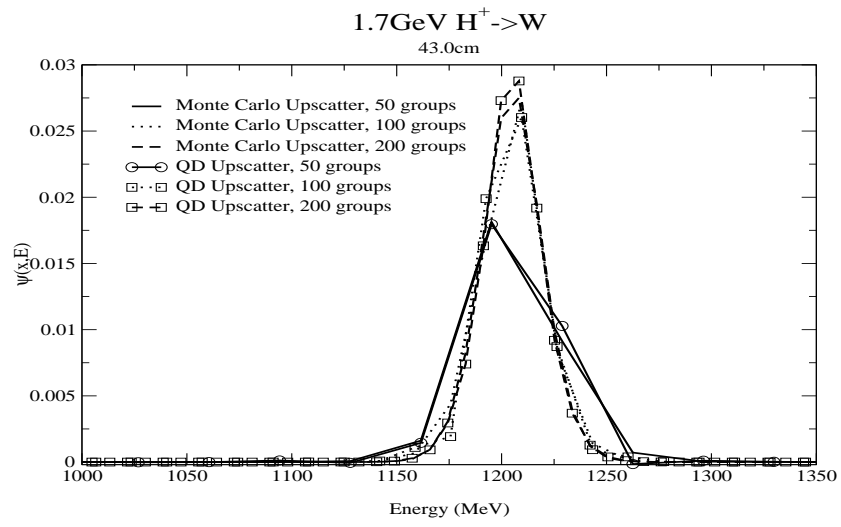


Figure 17: Quadratic discontinuous upscatter finite element group convergence for protons on tungsten at 43.0cm

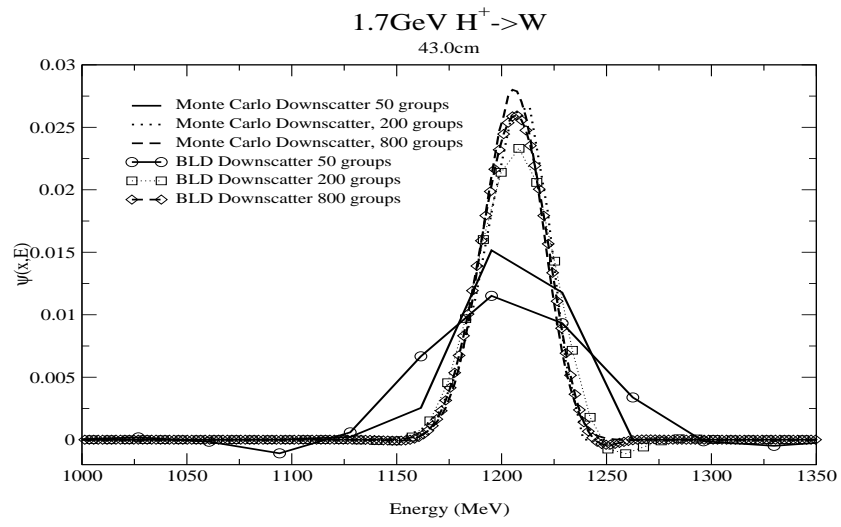


Figure 18: Bi-Linear discontinuous downscatter finite element group convergence for protons on tungsten at 43.0cm

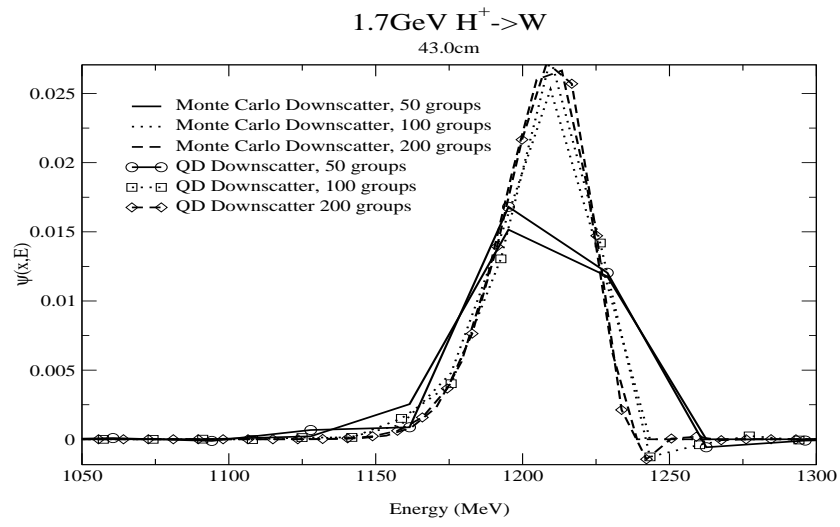


Figure 19: Quadratic discontinuous downscatter finite element group convergence for protons on tungsten at 43.0cm

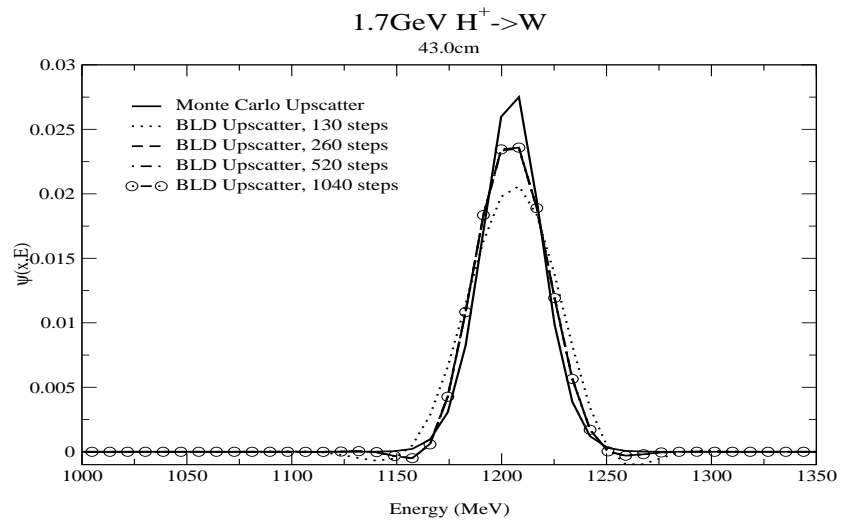


Figure 20: Bi-linear discontinuous upscatter finite element step convergence for protons on tungsten at 43.0cm

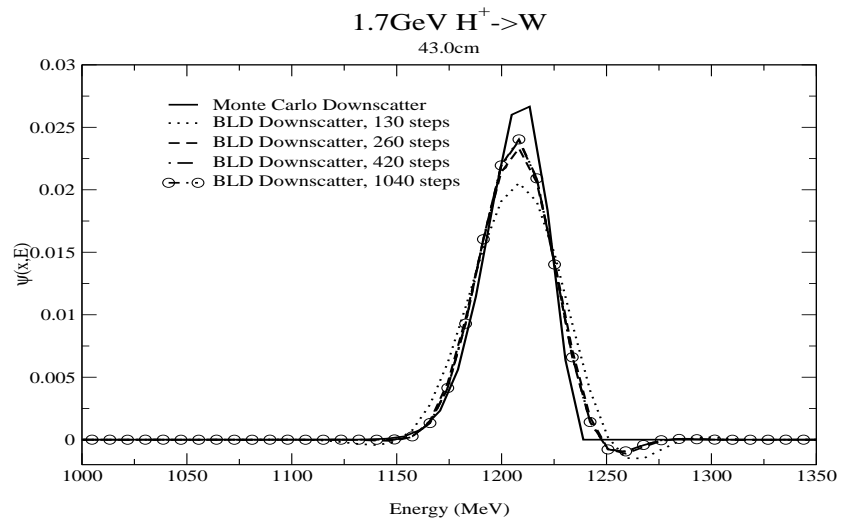


Figure 21: Bi-linear discontinuous downscatter finite element step convergence for protons on tungsten at 43.0cm

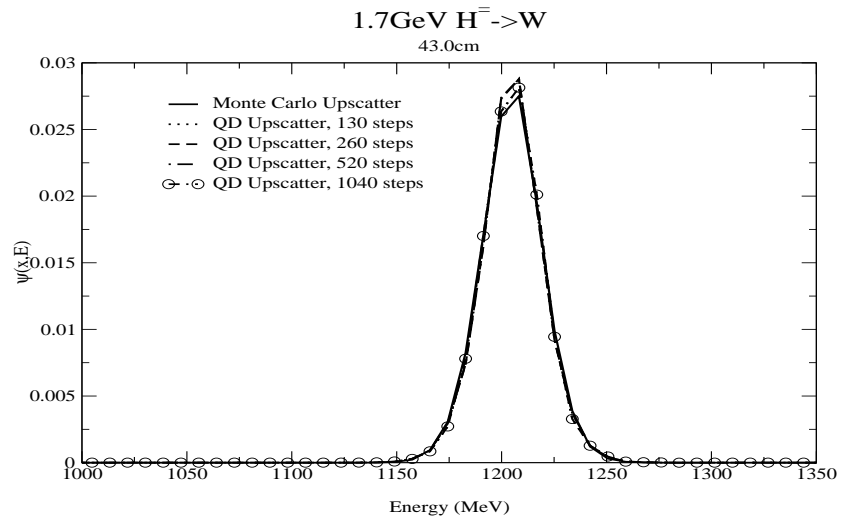


Figure 22: Quadratic discontinuous upscatter finite element step convergence for protons on tungsten at 43.0cm

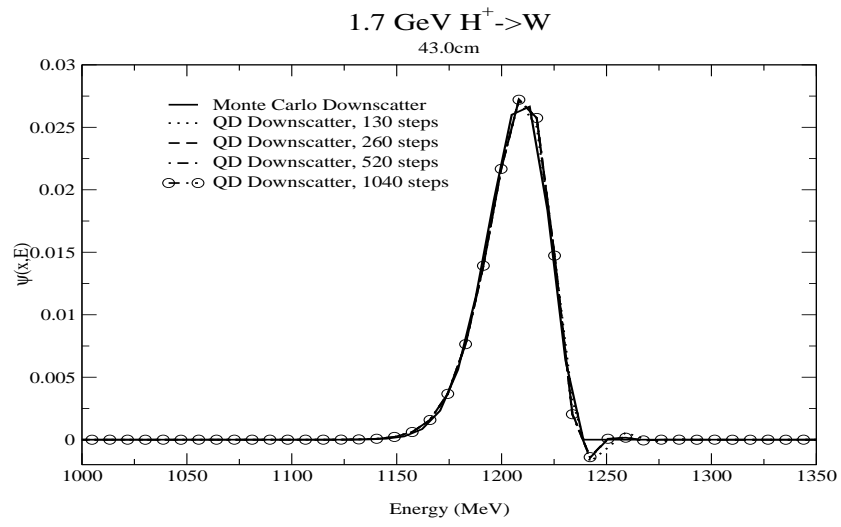


Figure 23: Quadratic discontinuous downscatter finite element step convergence for protons on tungsten at 43.0cm

6.2 Higher Order Methods

The finite element results for different order polynomial trial functions are compared against the respective Monte Carlo methods for a fixed spatial mesh and group structure. The comparisons show that accuracy gains are achieved with increasing polynomial order but not beyond the quadratic order. These results are shown in figure 24 and figure 25. The spectra is examined at 65.0cm in figures 24 and 25 where it has spread considerably from energy straggling. The energy group width is $\Delta E_g = 8.5\text{MeV}$ and the spatial mesh step is $\Delta x_k = 0.5\text{cm}$ for these two cases.

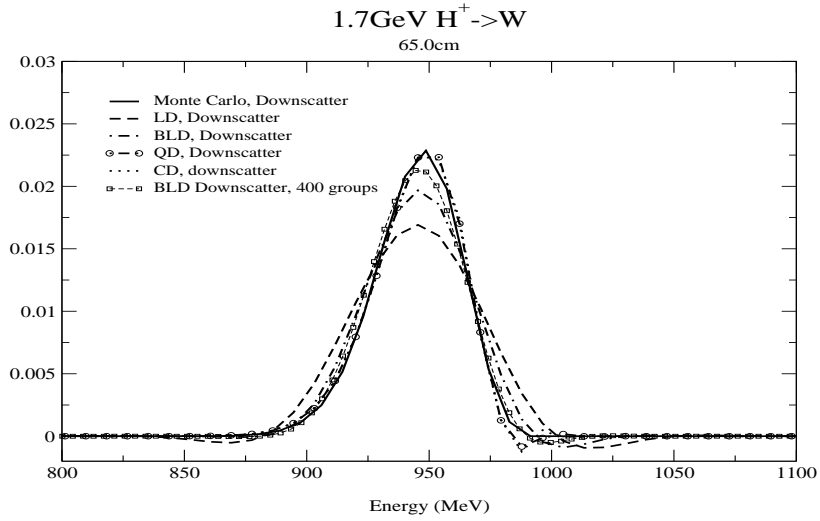


Figure 24: Discontinuous downscatter finite element method polynomial order convergence for protons on tungsten at 65.0cm

The figures 24 and 25 show that the BLD method must double the number of energy groups to be nearly as accurate as the QD method at half range. As shown in 16 and 18 the BLD method would require more groups at shallower depths to accurately capture the spectra.

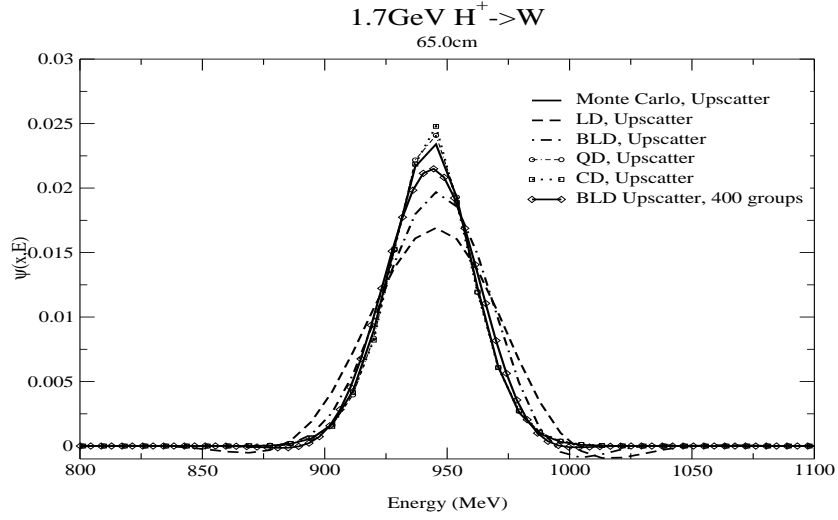


Figure 25: Discontinuous upscatter finite element polynomial order convergence for protons on tungsten at 65.0cm

When the group width cannot be sufficiently refined in places where highly accurate solutions are desirable, polynomials of order higher than the quadratic can often be used to good effect. An example is given in figure 26 displaying the spectra at 10.0cm. For a group width of 8.5MeV and spatial cell width of 0.5cm the quartic discontinuous (QT) method does better than the quadratic and cubic finite element results.

Figure 27 shows the effect of the removal of the bi-linear term and the small increase that the linear discontinuous (LD) finite element method shows when the strictly quadratic terms, i.e., the “ X^2 ” and “ E^2 ” terms, are added. As shown in figure 27 the gains made by the linear discontinuous finite element method with the extra quadratic terms are not as significant as the inclusion of the bi-linear cross term. Thus the cross terms play a significant role in resolving the peaked energy spectra, but all terms are necessary to achieve complete

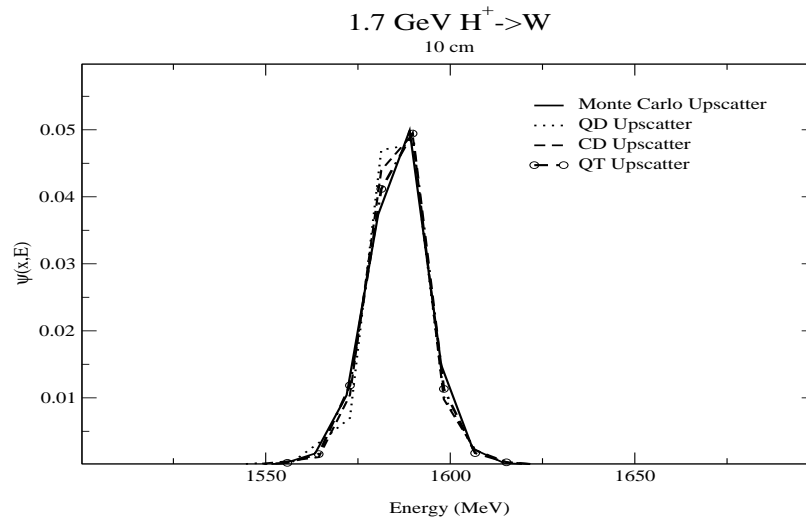


Figure 26: Discontinuous upscatter finite element polynomial order convergence for protons on tungsten at 10.0cm

accuracy.

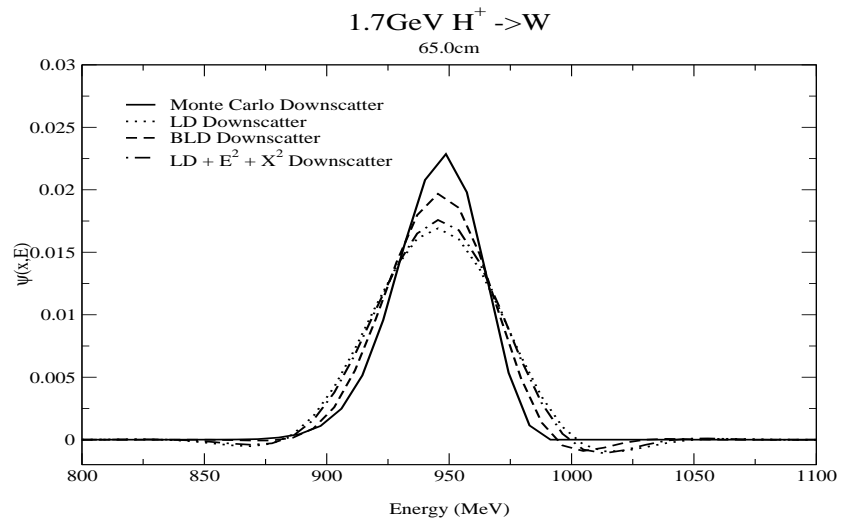


Figure 27: Cross Term comparison for discontinuous upscatter finite element for protons on tungsten at 65.0cm

6.3 Results for deep penetration

The finite element method was applied to the 1.7GeV protons on tungsten problem with $\Delta E_g = 8.54\text{MeV}$ and $\Delta x_k = 0.5\text{cm}$ and compared against the Monte Carlo multigroup method. The polynomial order of the finite element method needed is the full quadratic (with all cross terms in the trial function). The spectra was examined at the one-third, one-half, and two-thirds range.

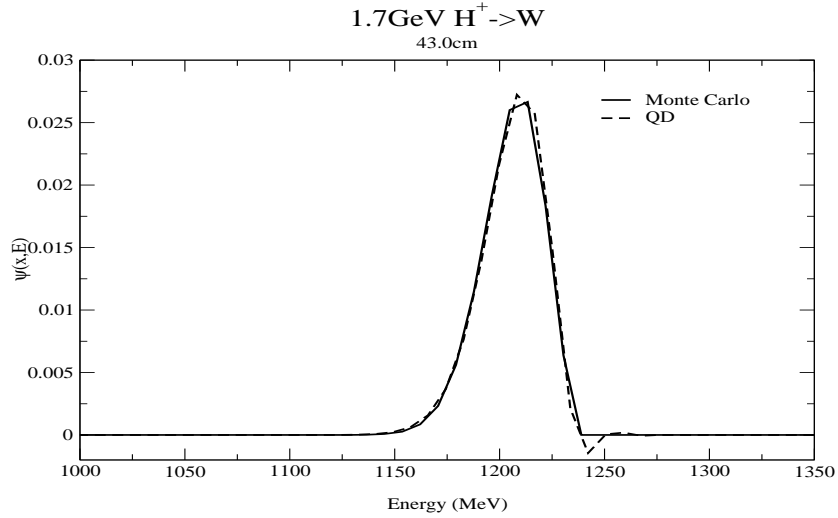


Figure 28: Quadratic discontinuous downscatter finite element method and downscatter Monte Carlo method for 1.7GeV protons on tungsten at 43.0cm.

These results are in excellent agreement with the Monte Carlo methods. For the 3.75MeV alpha particles on aluminum case, the finite element method is compared against the multigroup Monte Carlo method for the one-third, one-half, and two-thirds range. The finite element polynomial order was a full quadratic and the energy width was $\Delta E_g = 0.09967\text{ MeV}$ and the spacial width was $\Delta x_k = 1.0 \times 10^{-5}\text{cm}$.

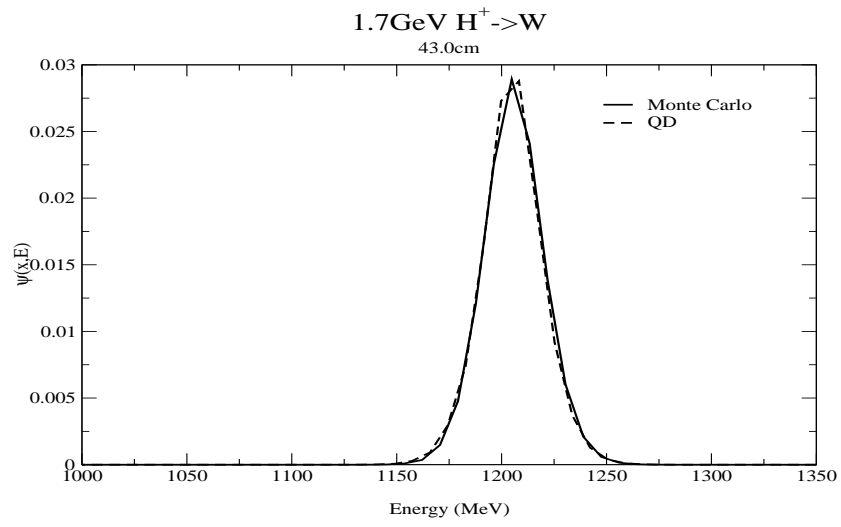


Figure 29: Quadratic discontinuous upscatter finite element method and upscatter Monte Carlo method for 1.7GeV protons on tungsten at 43.0cm.

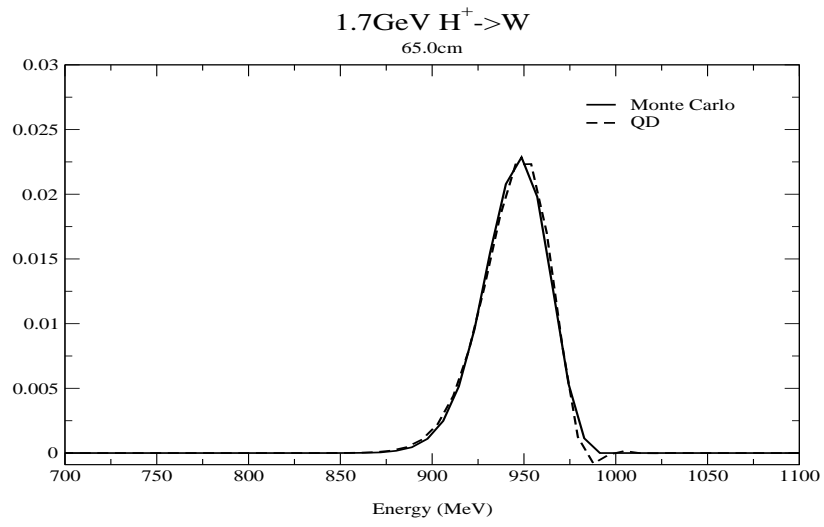


Figure 30: Quadratic discontinuous downscatter finite element method and downscatter Monte Carlo method for 1.7GeV protons on tungsten at 65.0cm.

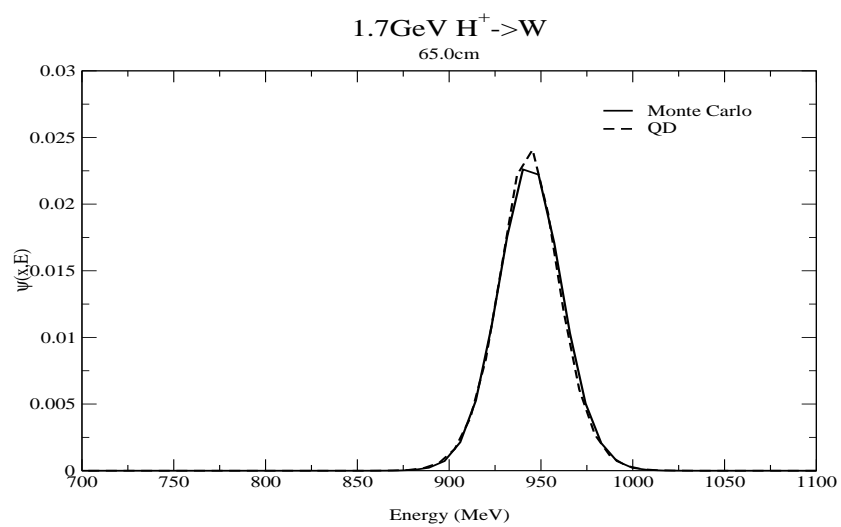


Figure 31: Quadratic discontinuous upscatter finite element method and downscatter Monte Carlo method for 1.7GeV protons on tungsten at 65.0cm.

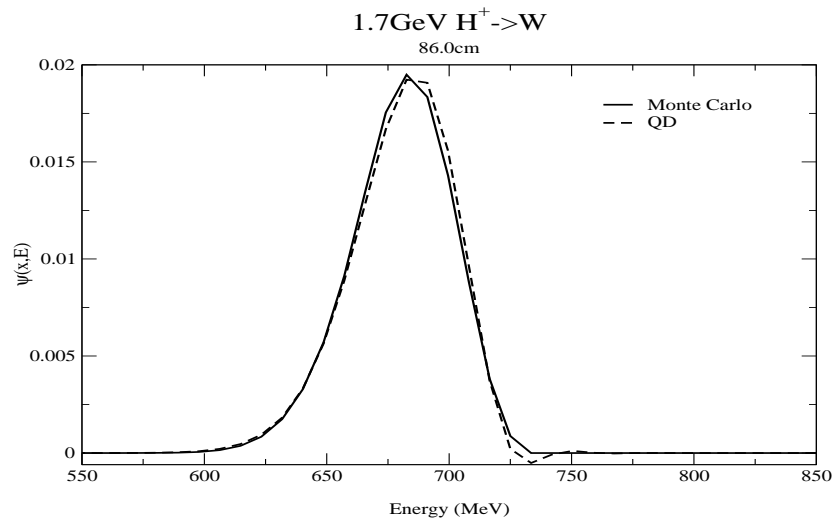


Figure 32: Quadratic discontinuous downscatter finite element method and downscatter Monte Carlo method for 1.7GeV protons on tungsten at 86.0cm.

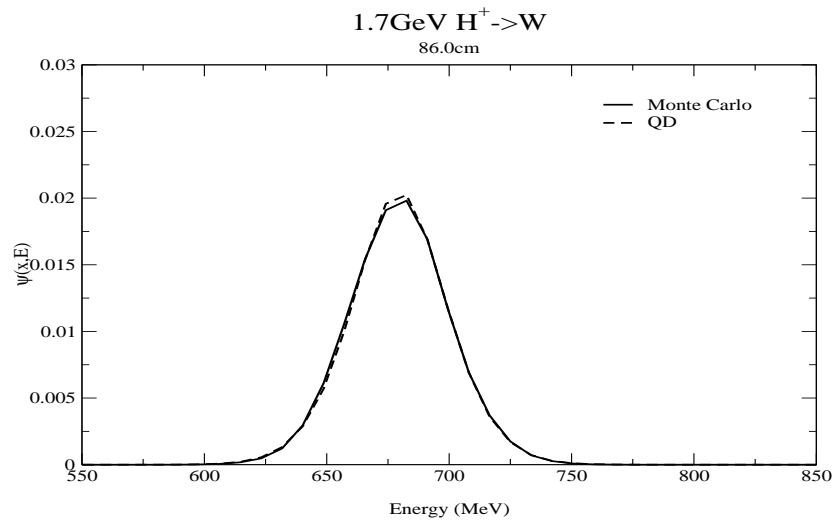


Figure 33: Quadratic discontinuous upscatter finite element method and upscatter Monte Carlo method for 1.7GeV protons on tungsten at 86.0cm.

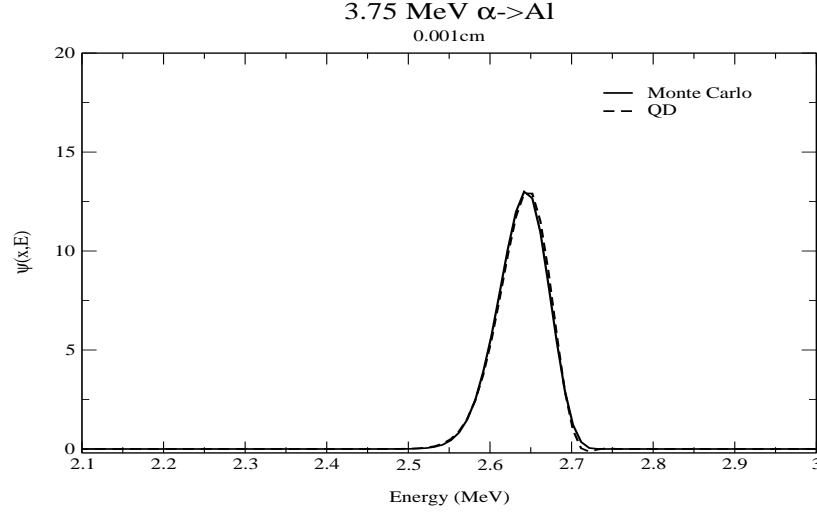


Figure 34: Quadratic discontinuous downscatter finite element method and downscatter Monte Carlo method for 3.75MeV alpha particles on aluminum at 0.001cm.

For the fusion alpha particles on aluminum problem, the negative oscillations experienced by the discontinuous finite element method are not evident. The oscillations disappear because the problem is dominated by mean and mean squared energy losses.

6.4 Dose and Ion Deposition

Results of energy deposition or dose were obtained for the 1.7GeV proton beam on tungsten and the 3.75MeV alpha particles on aluminum. All results show a characteristic Bragg peak. The expression for computing energy deposition is

$$D_k = \frac{1}{\Delta x_k} \int_{E_{min}}^{E_{max}} dE \int_{x_k - \frac{1}{2}}^{x_k + \frac{1}{2}} dx S(x, E) \Psi(x, E) \quad (54)$$

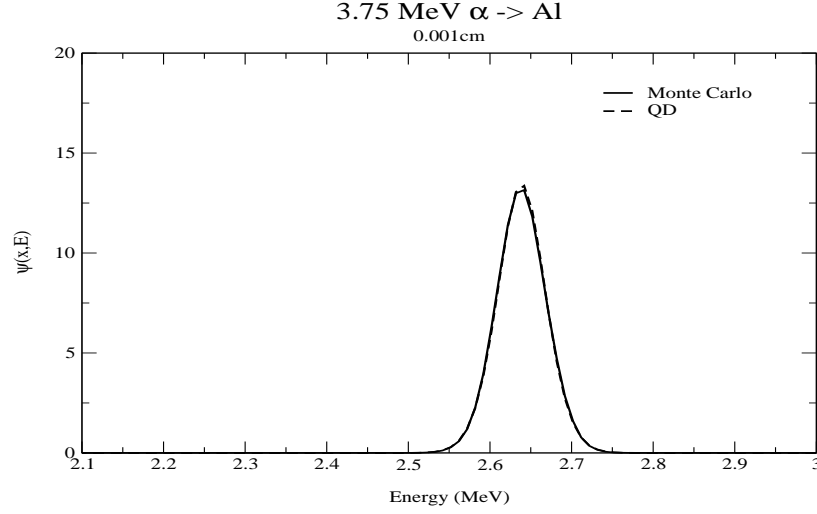


Figure 35: Quadratic discontinuous upscatter finite element method and upscatter Monte Carlo method for 3.75MeV alpha particles on aluminum at 0.001cm.

where D_k is the energy deposition for the k^{th} spatial point in units of MeV/cm. For the 1.7GeV proton beam on tungsten, the energy group width was 8.5 MeV and spacial cell width was 0.5 cm, and for the alpha particles on aluminum the energy group width was 0.1725 MeV and the spatial cell width was 1.0×10^{-5} cm. Both figure 39 and figure 40 display the dramatic difference resulting from including energy straggling in energy deposition calculations and the need for higher order polynomial trial functions for sufficiently crude energy grids. The Bragg peak for the CSD only case is very peaked while the energy straggled cases show broader Bragg peaks. This result has not been systematically demonstrated before.

The energy deposition results for the 3.75MeV alpha beam on aluminum display the dominance of the mean energy loss. In figure 41 and 42 the dose is sufficiently spread, so higher order polynomial trial functions add no extra

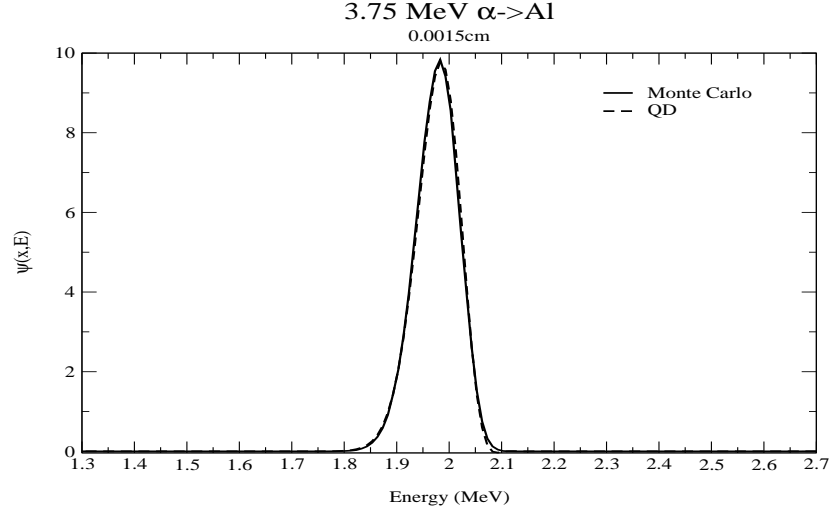


Figure 36: Quadratic discontinuous downscatter finite element method and downscatter Monte Carlo method for 3.75MeV alpha particles on aluminum at 0.0015cm.

resolution to the Bragg peak.

The ion deposition measures the spatial distribution of stopped ions in the target and can be obtained from the number of ions slowing down past the bottom energy group boundary and the number of ions straggling out of the bottom energy group. The ion deposition profile was calculated for protons on tungsten with energy group width was 8.5MeV and the spacial cell width was 0.5cm. For alpha particles on aluminum the energy group width was 0.1725 MeV and a spatial cell width was 1.5×10^{-5} cm. Figures 43 and 44 show that the ion deposition is converged at the quadratic polynomial order.

Table 3: Table of timings for multigroup upscatter methods

Method	Groups	Spatial	Upscatter Iterations	Upscatter Time (sec)
QD	200	260	14	116.61
BLD	200	260	14	27.76
LD	200	260	14	18.85
CD	200	260	14	396.12
QD	200	130	14	58.33
QD	200	520	14	233.49
QD	200	1040	14	471.02
QD	100	260	8	33.43
QD	50	260	6	12.66
QD	400	260	31	498.73
QD	800	260	76	2538.18
BLD	50	260	6	3.01
BLD	100	260	8	7.97
BLD	400	260	31	118.71
BLD	800	260	76	746.35
BLD	200	130	14	13.89
BLD	200	520	14	57.40
BLD	200	1040	14	112.65
Monte Carlo	200	-	-	326

Table 4: Table of timings for multigroup downscatter methods

Method	Groups	Spatial	Downscatter Time
QD	200	260	7.94
BLD	200	260	1.66
LD	200	260	1.01
CD	200	260	26.55
QD	50	260	1.95
QD	100	260	3.88
QD	400	260	15.42
QD	800	260	30.81
BLD	50	260	0.41
BLD	100	260	0.82
BLD	400	260	3.24
BLD	800	260	6.54
QD	200	130	3.86
QD	200	520	15.49
QD	200	1040	31.88
BLD	200	130	0.82
BLD	200	520	3.28
BLD	200	1040	6.53
Monte Carlo	200	-	228

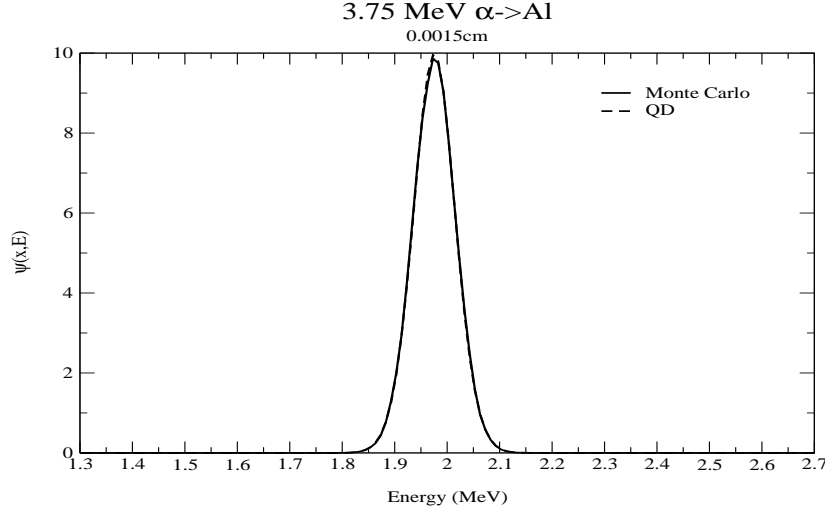


Figure 37: Quadratic discontinuous upscatter finite element method and upscatter Monte Carlo method for 3.75MeV alpha particles on aluminum at 0.0015cm.

6.5 Accuracy and Timings

Both the finite element upscatter and downscatter methods were timed for different ordered polynomial trial functions, refinement of the energy group mesh, and the refinement of the spacial mesh. As the upscatter iterations are increased the timings per individual iteration are roughly on the order of one downscatter run of the same type. Furthermore, for the 200 group mesh in downscatter QD finite element method the time is comparable to the 800 group downscatter BLD finite element method and for the upscatter QD finite element method the time is much less than the 800 group upscatter BLD method. The downscatter QD finite element method takes less time than its Monte Carlo counterpart while the upscatter QD finite element method is comparable to the upscatter Monte Carlo multigroup method. Thus much greater accuracy can be obtained for equivalent or less processor cost by applying higher order methods

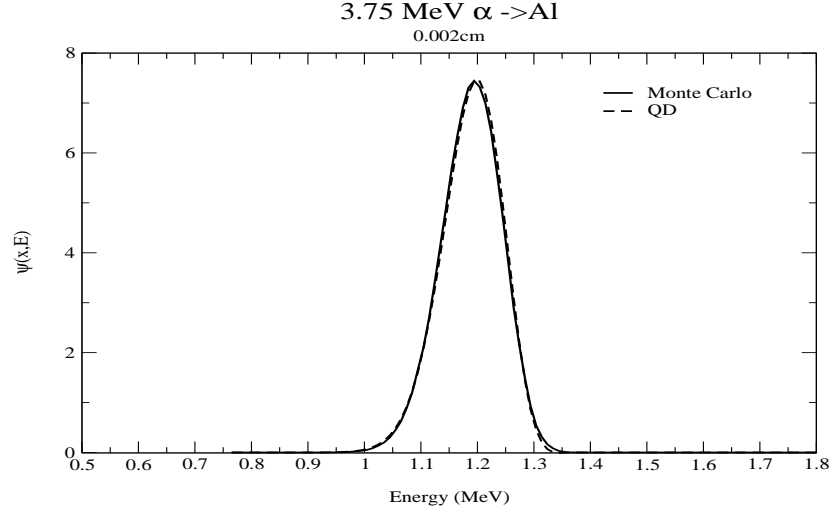


Figure 38: Quadratic discontinuous downscatter finite element method and downscatter Monte Carlo method for 3.75MeV alpha particles on aluminum at 0.002cm.

to a problem.

For the study on convergence the order of accuracy of a method is assumed to be proportional to one of the cell widths raised to some power α . Therefore if the convergence in space is examined as the number of spatial cells are increased the error of the solution decreases but at a rate determined by α . For this study the spacial order of convergence of the energy deposition is calculated. To obtain an estimate of the error, the different methods were compared against a super-converged solution. The expression for error is given by

$$\epsilon = \sqrt{\frac{\sum_{i=1}^{N_k} (D_{S.C.,i} - D_i)^2}{N_k}} \quad (55)$$

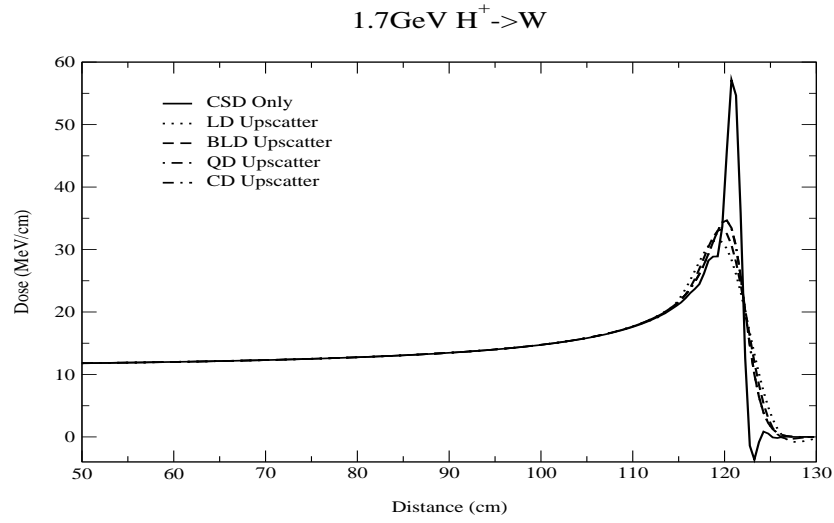


Figure 39: Discontinuous upscatter finite element method dose profiles for 1.7GeV protons on tungsten

The results for the rate of convergence are given in table 5, and as shown the higher the polynomial method the faster the rate of convergence. Significantly, the expected theoretical orders of accuracy in one dimension are evidently approached.

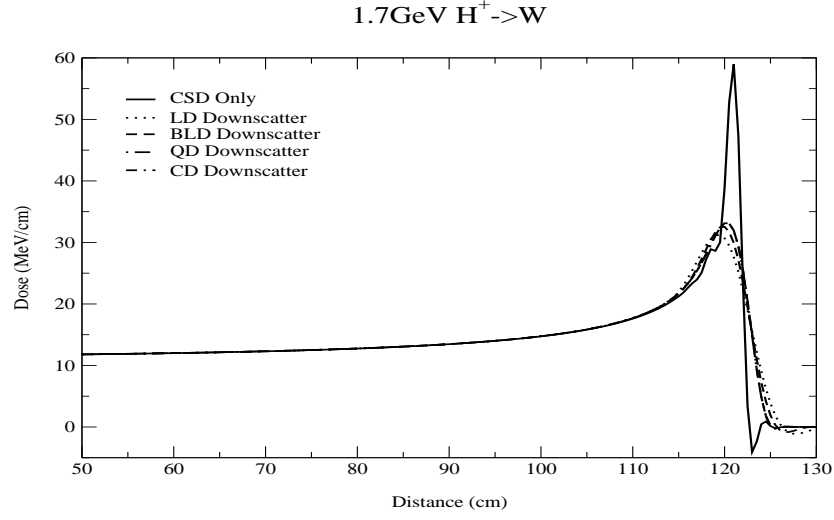


Figure 40: Discontinuous downscatter finite element method dose profiles for 1.7GeV protons on tungsten

Table 5: L_2 errors and Spatial Order of Accuracy for Dose and were measured over a 150 cm domain.

K	LD	BLD	QD	CD
150	0.864277	0.415089	2.67686×10^{-2}	5.35090×10^{-3}
300	0.417809	7.77502×10^{-2}	1.16599×10^{-3}	8.47745×10^{-4}
600	0.177604	1.04230×10^{-2}	3.82016×10^{-5}	8.80775×10^{-6}
1200	5.82839×10^{-2}	1.17423×10^{-3}	1.16730×10^{-6}	7.11871×10^{-8}
Order α	1.20904	2.8291	4.8387	6.7699

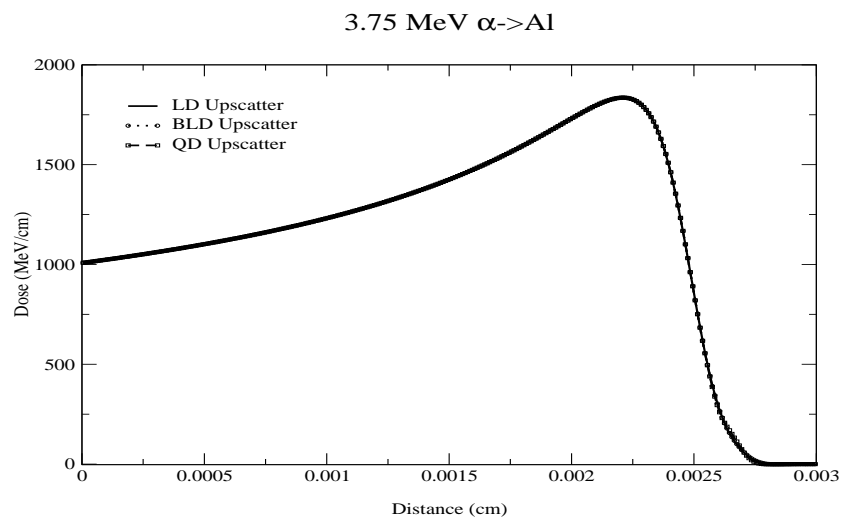


Figure 41: Discontinuous upscatter finite element method dose profiles for 3.75MeV alphas on aluminum

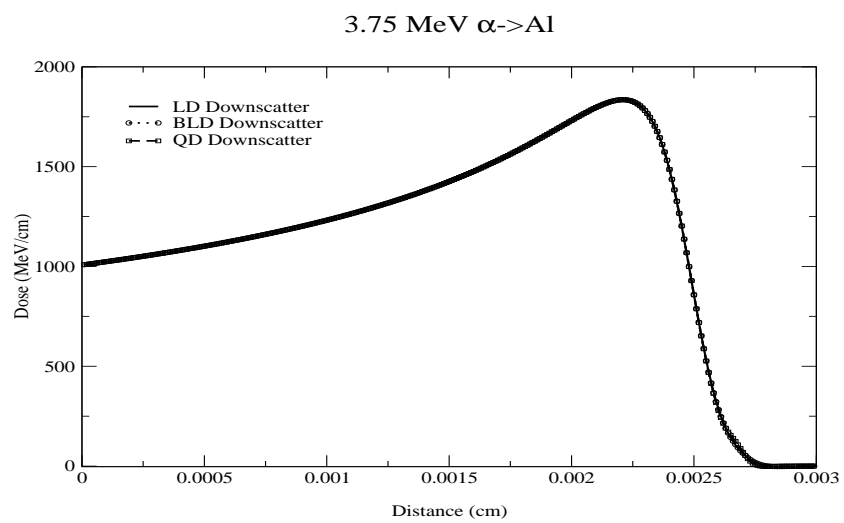


Figure 42: Discontinuous downscatter finite element method dose profiles for 3.75MeV alphas on aluminum

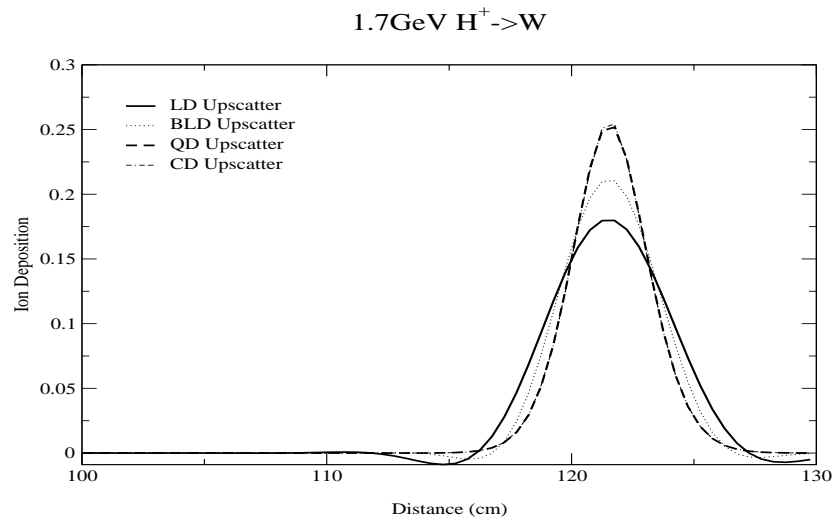


Figure 43: Discontinuous upscatter finite element method ion deposition profiles for 1.7GeV protons on tungsten

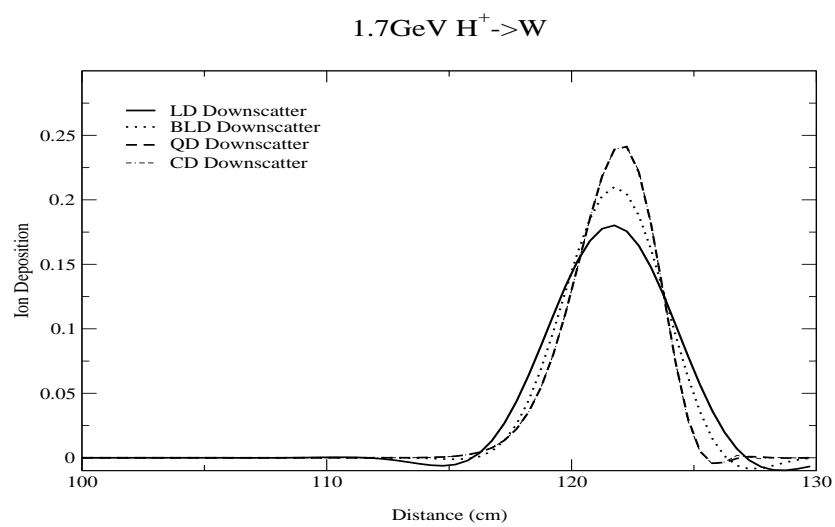


Figure 44: Discontinuous downscatter finite element method ion deposition profiles for 1.7GeV protons on tungsten

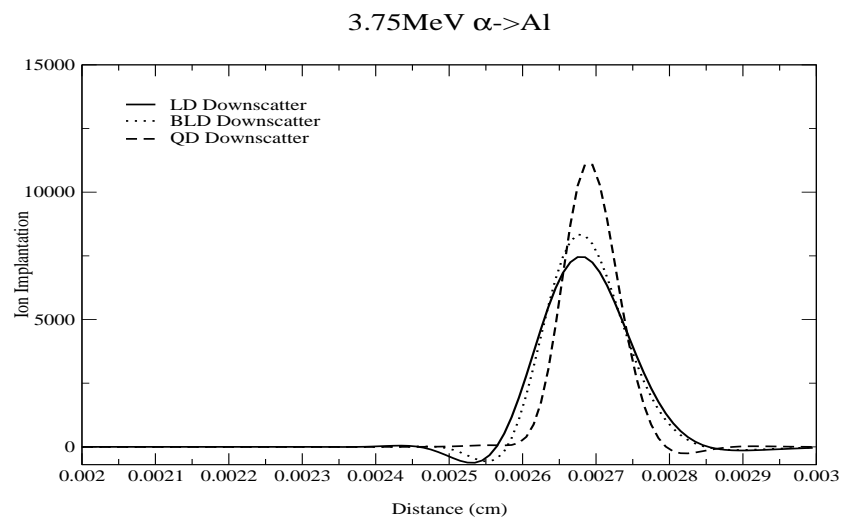


Figure 45: Discontinuous downscatter finite element method ion deposition profiles for 3.75MeV alpha particles on aluminum

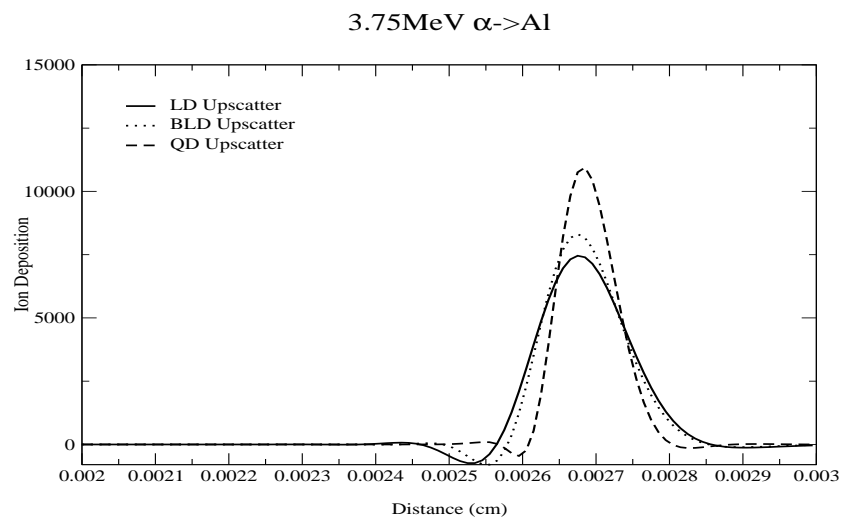


Figure 46: Discontinuous upscatter finite element method ion deposition profiles for 3.75MeV alpha particles on aluminum

7 Arbitrary Order Nonlinear Discontinuous Finite Element Methods

While the linear family of arbitrary degree polynomial discontinuous finite element methods were shown to yield accurate results, with efficiency, for the challenging class of problems investigated here, a lack of robustness was evident for spectra at very shallow depths. The extreme peakedness of these solutions resulted in occasional oscillations in the tails, although the use of discontinuous trial functions greatly mitigated this effect. In this section, we propose a novel method which gives guaranteed positive numerical solutions while retaining high accuracy. Accuracy and positivity is achieved, however, at the expense of nonlinearity and hence computational expediency, but the scheme has much scope for optimization, suitable for future study. Here we demonstrate the method on our downscatter transport model and contrast it against the linear finite element approach of the previous sections.

Our basic ansatz is that the trial functions can be represented as expansions in arbitrary degree polynomials in space and energy but with the expansion appearing in the exponent of the exponential function. The grid unknowns are the polynomial expansion coefficients so that the trial functions are nonlinear functions of these unknowns. As the exponential is a positive definite function, it follows that positive solutions will result for positive sources. However, the system of equations for the grid unknown will be nonlinear and must be iteratively relaxed. We present the essential details below.

Applying the Galerkin procedure to the downscatter-only effective transport equation, we obtain

$$\langle \omega_{a',b'} | L(\Psi) - Q \rangle = 0, a' = 0 \cdots A, b' = 0 \cdots B$$

where

$$L() = \mu_n \frac{\partial}{\partial x} - \frac{\partial}{\partial E} S(x, E) + \sigma_{g \rightarrow g'} \quad (56)$$

and

$$Q = \int_E^{E_{max}} dE' \frac{\sigma_{g-1 \rightarrow g}}{\Delta E_g} \Psi(x, E) \quad (57)$$

where a' and b' are the order indices for the weight function ω . The weak form that results from the multiplication is

$$\begin{aligned} & \int_g \Psi(x, E) \big|_{k+\frac{1}{2}} \omega(E, x) \big|_{k+\frac{1}{2}} - \int_g \Psi(x, E) \big|_{k-\frac{1}{2}} \omega(E, x) \big|_{k-\frac{1}{2}} \\ & - \int_k \int_g \frac{\partial \omega}{\partial x} \Psi(x, E) dE dx - \int_k (S(x, E) \Psi(x, E)) \big|_{g-\frac{1}{2}} \omega(E, x) \big|_{g-\frac{1}{2}} dx \\ & \int_k (S(x, E) \Psi(x, E)) \big|_{g+\frac{1}{2}} \omega(E, x) \big|_{g+\frac{1}{2}} dx + \int_k \int_g (S(x, E) \Psi(x, E)) \frac{\partial \omega}{\partial E} dE dx \\ & + \int_k \int_g \sigma_{g \rightarrow g'} \Psi^A(x, E) \omega(E, x) dx = \int_k \int_g \int_{g-1} \frac{\sigma_{g-1 \rightarrow g}}{\Delta E_g} \Psi(x, E') dE' \omega(E, x) dE dx \end{aligned} \quad (58)$$

We insist that the trial functions be discontinuous at the cell inflow boundaries for enhanced accuracy and robustness in the solution. For every element g, k the weak form with the discontinuities in space and energy is given by

$$\begin{aligned} & \int_g \Psi(x, E) \big|_{k+\frac{1}{2}} \omega(E, x) \big|_{k+\frac{1}{2}} - \int_g \Psi(x, E) \big|_{k-1} \omega(E, x) \big|_{k-\frac{1}{2}} \\ & - \int_k \int_g \frac{\partial \omega}{\partial x} \Psi(x, E) dE dx - \int_k (S(x, E) \Psi(x, E)) \big|_{g-1} \omega(E, x) \big|_{g-\frac{1}{2}} dx \\ & \int_k (S(x, E) \Psi(x, E)) \big|_{g+\frac{1}{2}} \omega(E, x) \big|_{g+\frac{1}{2}} dx + \int_k \int_g (S(x, E) \Psi(x, E)) \frac{\partial \omega}{\partial E} dE dx \\ & + \int_k \int_g \sigma_{g \rightarrow g'} \Psi^A(x, E) \omega(E, x) dx = \int_k \int_g \int_{g-1} \frac{\sigma_{g-1 \rightarrow g}}{\Delta E_g} \Psi(x, E') dE' \omega(E, x) dE dx \end{aligned} \quad (59)$$

The weight functions are taken from the space of low order polynomials, specifically Legendre polynomials, given as before by

$$\omega(x, E)_{a', b'} = p_{a'}(x)p_{b'}(E) \quad (60)$$

where the definitions of the polynomials are given in expression 43. The trial functions, on the other hand, are expressed as nonlinear exponential functions in each 2D cell (k, g) , of the form

$$\Psi(x, E) \approx \exp \left[\sum_{a=0}^A \sum_{b=0}^B p_a(x)p_b(E)\lambda_{k,g}^{a,b} \right] \quad (61)$$

where $\lambda_{k,g}^{a,b}$ are the grid unknowns. Substituting the weight function and trial function for each g, k element yields

$$\begin{aligned} & \int_g \sum_{a=0}^A \sum_{b=0}^B \lambda_{a,b}^{k,g} (1)^a p_b^g(E) p_b^g(E) dE - \int_g (-1)^n e^{\sum_{a=0}^A \sum_{b=0}^B \lambda_{a,b}^{k,g-1} (1)^a p_b^g(E)} p_b^g(E) dE \\ & - \int_k \int_g \frac{\partial p_{a'}^k(x)}{\partial x} p_b^g(E) e^{\sum_{a=0}^A \sum_{b=0}^B \lambda_{a,b}^{k,g} p_a^k(x) p_b^g(E)} dE dx \\ & - \int_k S_{k,g-1} e^{\sum_{a=0}^A \sum_{b=0}^B \lambda_{a,b}^{k,g-1} p_a^k(x) (-1)^b} p_{a'}^k(x) dx \\ & + \int_k (-1)^b S_{k,g} e^{\sum_{a=0}^A \sum_{b=0}^B \lambda_{a,b}^{k,g} p_a^k(x) (-1)^b} p_{a'}^k(x) dx \\ & + \int_k \int_g S_{k,g} e^{\sum_{a=0}^A \sum_{b=0}^B \lambda_{a,b}^{k,g} p_a^k(x) p_b^g(E)} \frac{\partial p_{b'}^g(E)}{\partial E} dE p_{a'}^k(x) dx \\ & + \int_k \int_g \sigma_{k,g \rightarrow g'} e^{\sum_{a=0}^A \sum_{b=0}^B \lambda_{a,b}^{k,g} p_a^k(x) p_b^g(E)} p_{b'}^g(E) p_{a'}^k(x) dx \\ & - \int_k \int_g \int_{g-1} \frac{\sigma_{k,g-1}}{\Delta E_g} e^{\sum_{a=0}^A \sum_{b=0}^B \lambda_{a,b}^{k,g-1} p_a^k(x) p_b^{g-1}(E)} dE' p_{b'}^g(E) dE p_{a'}^k(x) dx = 0 \end{aligned} \quad (62)$$

The integrals for orders higher than pure linear in the exponent (i.e., without the bilinear and higher terms) cannot be carried out in closed form. We use low order Gauss quadrature to perform all integrals and a multidimensional Newton's method to relax the resulting nonlinear system of algebraic equations for the grid unknowns.

7.1 Multidimensional Newton's Method

There are many excellent references on solving systems of nonlinear equations, e.g., [17, 18]. Here we give a brief recap of the multidimensional Newton method for solving a system of nonlinear equations given by

$$\begin{aligned}
f_1(x_1, x_2, x_3, x_4, \dots, x_N) &= 0 \\
f_2(x_1, x_2, x_3, x_4, \dots, x_N) &= 0 \\
f_3(x_1, x_2, x_3, x_4, \dots, x_N) &= 0 \\
f_4(x_1, x_2, x_3, x_4, \dots, x_N) &= 0 \\
&\vdots \\
f_N(x_1, x_2, x_3, x_4, \dots, x_N) &= 0
\end{aligned} \tag{63}$$

where there are N equations with N variables. Like the scalar Newton method, the root can be found by iterating on the independent variable with information from the function and the function's slope. The method begins by setting the initial iterate to a guess and then evaluating the function's slope. The intersection to the variables axis is obtained and becomes the next guess or iterate. The process continues until a zero is found within acceptable tolerance.

For a multidimensional nonlinear system, of the type of interest here, the corrections are obtained from the intersections of the tangent. The corrections are then added to the guess to form new iterates. The process iterates until a root is found within acceptable tolerance. To obtain the iterate corrections a Taylor's series expansion is performed on all the nonlinear relations f_j . The

Taylor expansion of the j th equation, f_j is

$$f_j(x_1, x_2, x_3, x_4, \dots, x_N) = f_0 + \frac{\partial f_j}{\partial x_1} \Delta x_1 + \frac{\partial f_j}{\partial x_2} \Delta x_2 + \frac{\partial f_j}{\partial x_3} \Delta x_3 + \frac{\partial f_j}{\partial x_4} \Delta x_4 \dots + \frac{\partial f_j}{\partial x_N} \Delta x_N + O(\Delta x^2) \quad (64)$$

where Δx_i is the difference centered about the root for x_i . The Taylor expansion of $f_j(x_1, x_2, x_3, x_4, \dots, x_N) = 0$ which means that

$$\frac{\partial f_j}{\partial x_1} \Delta x_1 + \frac{\partial f_j}{\partial x_2} \Delta x_2 + \frac{\partial f_j}{\partial x_3} \Delta x_3 + \frac{\partial f_j}{\partial x_4} \Delta x_4 \dots + \frac{\partial f_j}{\partial x_N} \Delta x_N = -f_0 \quad (65)$$

when the $O(\Delta x^2)$ are truncated from the Taylor expansion. In matrix form the equations are expressed as

$$\begin{bmatrix} \frac{\partial f_1}{\partial x_1} & \frac{\partial f_1}{\partial x_2} & \frac{\partial f_1}{\partial x_3} & \frac{\partial f_1}{\partial x_4} & \dots & \frac{\partial f_1}{\partial x_N} \\ \frac{\partial f_2}{\partial x_1} & \frac{\partial f_2}{\partial x_2} & \frac{\partial f_2}{\partial x_3} & \frac{\partial f_2}{\partial x_4} & \dots & \frac{\partial f_2}{\partial x_N} \\ \frac{\partial f_3}{\partial x_1} & \frac{\partial f_3}{\partial x_2} & \frac{\partial f_3}{\partial x_3} & \frac{\partial f_3}{\partial x_4} & \dots & \frac{\partial f_3}{\partial x_N} \\ \frac{\partial f_j}{\partial x_1} & \frac{\partial f_j}{\partial x_2} & \frac{\partial f_j}{\partial x_3} & \frac{\partial f_j}{\partial x_4} & \dots & \frac{\partial f_j}{\partial x_N} \\ \vdots & \vdots & \vdots & \vdots & \dots & \vdots \\ \frac{\partial f_N}{\partial x_1} & \frac{\partial f_N}{\partial x_2} & \frac{\partial f_N}{\partial x_3} & \frac{\partial f_N}{\partial x_4} & \dots & \frac{\partial f_N}{\partial x_N} \end{bmatrix} \begin{bmatrix} \Delta x_1 \\ \Delta x_2 \\ \Delta x_3 \\ \Delta x_j \\ \vdots \\ \Delta x_N \end{bmatrix} = \begin{bmatrix} -f_1 \\ -f_2 \\ -f_3 \\ -f_j \\ \vdots \\ -f_N \end{bmatrix}$$

Gauss elimination or LU decomposition is then applied to the matrix, and the corrections to the iterate are obtained. The corrections are then applied to the iterate and a new iterate is obtained. This is expressed as

$$x_i^{k+1} = x_i^k + \Delta x_i^k \quad (66)$$

Where k is the iteration index and i is the i th variable for the root. The method continues to iterate until a root is obtained within a preset tolerance, with convergence determined according to the L_2 -norm for the residual

$$\sqrt{\sum_{j=1}^N \langle \omega_j | L(v) - f \rangle_{g,k}^2} < \epsilon \quad (67)$$

where ω_j is the $a'b'$ weight function and v is the exponential trial function given by Eq.61.

8 Numerical Results of Nonlinear Methods

In this section, we present numerical results from the implementation of the nonlinear exponential discontinuous finite element method to the straggling of 1.7GeV protons in tungsten. The results and analysis is brief and is by no means exhaustive; there is much scope for future work in order to gain greater understanding of the method. For the results presented here, uniform energy groups and spacial cells have been used, with a group width of 8.5MeV and a spatial mesh width of 1cm.

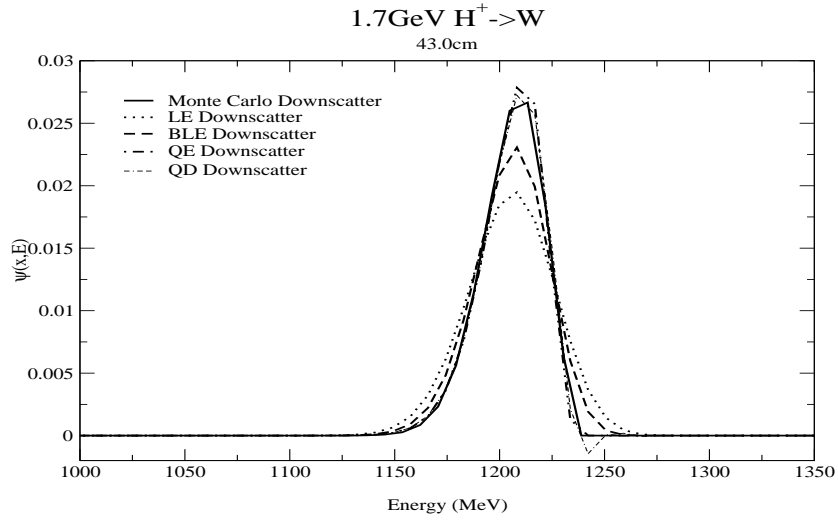


Figure 47: Discontinuous downscatter exponential finite element method polynomial order convergence for protons on tungsten at 43.0cm

As expected the exponential discontinuous finite element method yields monotone positive results, with the exponential quadratic (QE) solution agreeing extremely well with the Monte Carlo and QD downscatter results. As shown in figures 47, 48, and 49 all orders converge to the QE result for the depths considered. Clearly, the absence of any negativities is a highly desirable and

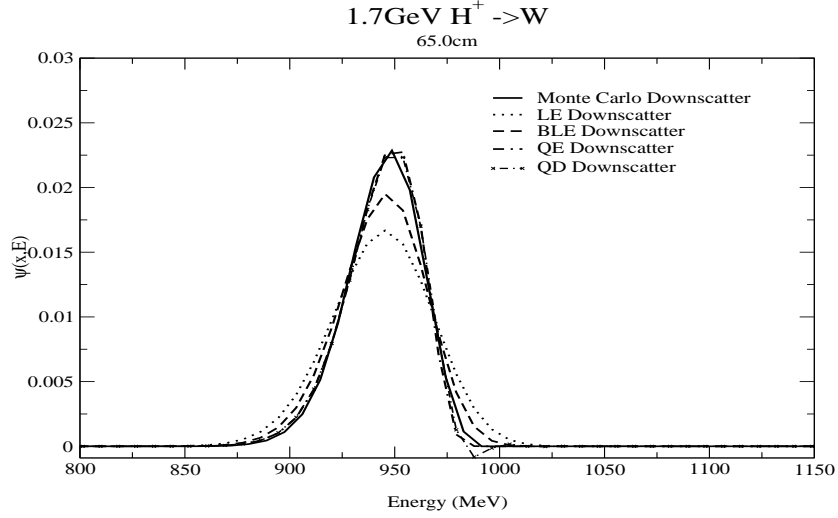


Figure 48: Discontinuous exponential downscatter finite element method polynomial order convergence for protons on tungsten at 65.0cm

superior property of the nonlinear scheme.

The impact of straggling on spreading out the Bragg peak is also strongly evident with these methods. The higher order exponential methods capture the Bragg peak height very closely while remaining positive, and the lower orders show a decreased peak height with a greater spread.

The results shown in Table 6 indicate that the exponential method is extremely expensive when compared to the downscatter finite element method of the same polynomial order in the linear family. This is not surprising given the quadrature and Newton iterations that are required in the nonlinear method. The quadrature order is higher for the higher order methods (typically 18 for QE in contrast to 8 for BLE) and appears to be related to the flexibility of the higher order polynomials in representing sharply varying solutions. Obviously, more research must be done to optimize the exponential discontinuous method

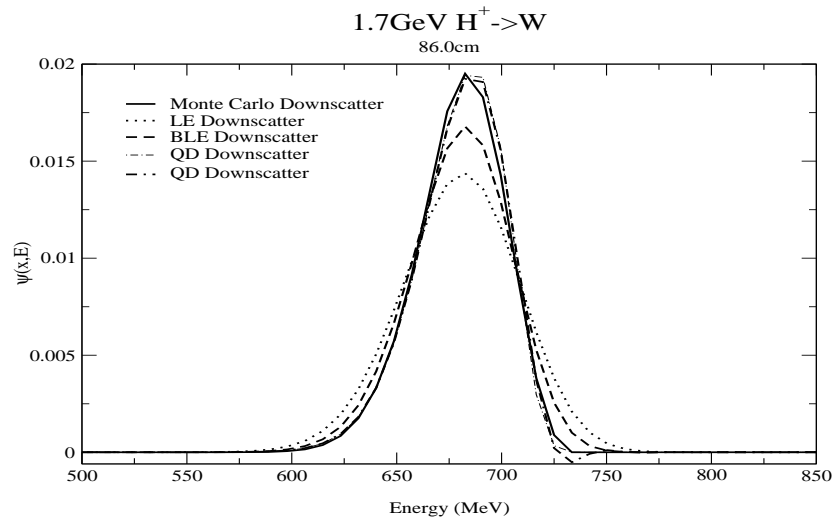


Figure 49: Discontinuous downscatter finite element method polynomial order convergence for protons on tungsten at 86.0cm

so as to make it competitive with other linear element techniques, but clearly we have shown intriguing possibilities.

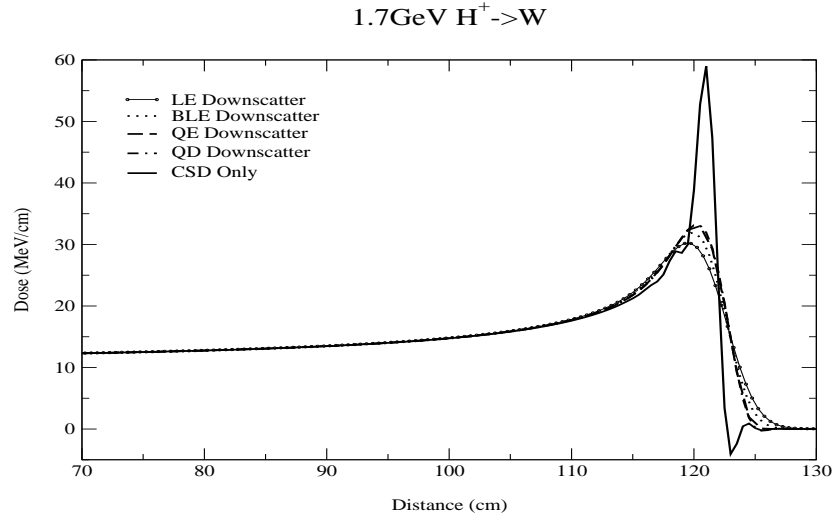


Figure 50: Discontinuous downscatter exponential finite element dose results for 1.7GeV protons on tungsten

Table 6: Timing results for arbitrary polynomial exponential discontinuous finite element method for 1.7GeV protons on tungsten target

Method	Average Newton Iterations	Total Time	Quadrature Order
LE	18	521.289	4
BLE	19	1464.240	6
QE	25	2.88×10^4	18

References

- [1] K. Krane. *Introductory Nuclear Physics*. Wiley, New York, 1988.
- [2] R. Evans. *The Atomic Nucleus*. McGraw-Hill, New York, 1955.
- [3] J. Janni. "Proton Range-Energy Tables, 1keV-10GeV". *Atomic Data and Nuclear Data Tables*, 27:147–339, March 1982.
- [4] J.E Turner. *Atoms, Radiation, and Radiation Protection*. McGRAW-HILL INC., New York, 1986.
- [5] S. Ahlen. "Theoretical and experimental aspects of the energy loss of relativistic heavy ionizing particles". *Reviews of Modern Physics*, 52(1):121–173, 1980.
- [6] Q. Yang, D. Connor, and Z. Wang. "Empirical formulae for energy loss straggling of ions in matter". *Nuclear Instruments and Methods in Physics Research*, pages 149–155, 1991.
- [7] M. Payne. "Energy Straggling of Heavy Charged Particles in Thick Absorbers". *Physical Review*, 185:611–623, 1969.
- [8] A. Prinja, F. Gleicher, and J. Morel. "A Multigroup, Downscatter-Only Model for Charged Particle Energy Straggling". In *Proceedings of the International Conference on Mathematics and Computation, Reactor Physics and Environmental Analyses in Nuclear Applications*. Proceedings of the International Conference on Mathematics and Computation, Reactor Physics and Environmental Analyses in Nuclear Applications, September 1999.
- [9] P.W. Lisowski. "The Accelerator Production of Tritium Project". In *1997 IEEE Particle Accelerator Conference*, volume 3. IEEE, May 1997.
- [10] A. Prinja and L. Lorence. "Exponential Discontinuous Numerical Scheme for Electron Transport in the Continuous Slowing Down Approximation".

In *Joint International Conference on Mathematical Methods and Supercomputing for Nuclear Applications*, volume 2. American Nuclear Society, October 1997.

- [11] J. Reddy. *Finite Element Method*. McGraw-Hill, New York, 1993.
- [12] R.E. White. *An Introduction to the Finite Element Method with Applications to Nonlinear Problems*. John Wiley and Sons Inc., New York, USA, 1985.
- [13] A. Davies. *The Finite Element Method*. Claredon Press, Oxford, New York, USA, 1980.
- [14] O.C. Zienkiewicz. *The Finite Element Method in Engineering Science*. McGraw-Hill Ltd., London, England, 1971.
- [15] E. Kreyszig. *Advanced Engineering Mathematics*. John Wiley and Sons Inc., New York, 1993.
- [16] Joel Turinetti. A Quadratic Discontinuous Finite Element Solution of the Fokker-Planck Transport Equation for Charged Particles. Master's thesis, University of New Mexico, 1999.
- [17] J. Hoffman. *Numerical Methods for Engineers and Scientists*. McGraw-Hill, 1992.
- [18] Gerald and Wheatly. *Applied Numerical Analysis, Fifth Ed.* Addison-Wesley Publishing Company, Inc., New York, 1994.